ACOUSTIC IMPEDANCE INVERSION OF LOWER PERMIAN CARBONATE BUILDUPS IN THE PERMIAN BASIN, TEXAS

A Thesis

by

PABLO BUENAFAMA ALEMAN

Submitted to the Office of Graduate Studies of
Texas A&M University
in partial fulfillment of the requirements for the degree of

MASTER OF SCIENCE

August 2004

Major Subject: Geophysics

ACOUSTIC IMPEDANCE INVERSION OF LOWER PERMIAN CARBONATE BUILDUPS IN THE PERMIAN BASIN, TEXAS

A Thesis

by

PABLO BUENAFAMA ALEMAN

Submitted to Texas A&M University
in partial fulfillment of the requirements
for the degree of

MASTER OF SCIENCE

Approved as to style and content by:

Richard L. Gibson (Chair of Committee)	Steven Dorobek (Member)
Duane A. McVay (Member)	Richard Carlson (Head of Department)

August 2004

Major Subject: Geophysics

ABSTRACT

Acoustic Impedance Inversion of Lower Permian
Carbonate Buildups in the Permian Basin, Texas. (August 2004)
Pablo Buenafama Aleman, B.S., Simon Bolivar University
Chair of Advisory Committee: Dr. Richard L. Gibson

Carbonate reservoirs are usually difficult to map and identify in seismic sections due to their complex structure, lithology and diagenetic frabrics. The Midland Basin, located in the Permian Basin of West Texas, is an excellent example of these complex carbonate structures.

In order to obtain a better characterization and imaging of the carbonate buildups, an acoustic impedance inversion is proposed here. The resolution of the acoustic impedance is the same as the input seismic data, which is greatly improved with the addition of the low frequency content extracted from well data. From the broadband volume, high resolution maps of acoustic impedance distributions were obtained, and therefore the locations of carbonate buildups were easily determined. A correlation between acoustic impedance and porosity extracted from well data shows that areas with high acoustic impedance were correlated with low porosity values, whereas high porosities were located in areas of low acoustic impedance.

Theoretical analyses were performed using the time-average equation and the Gassmann equation. These theoretical models helped to understand how porosity distributions affect acoustic impedance. Both equations predicted a decrease in acoustic impedance as porosity increases. Inversion results showed that average porosity values are $5\% \pm 5\%$, typical for densely cemented rocks. Previous studies done in the study area indicate that grains are moderately to well-sorted. This suggests that time-average approximation will overestimate porosity values and the Gassmann approach better predicts the measured data. A comparison between measured data and the Gassmann equation suggests that rocks with low porosities (less than 5%) tend to have high acoustic impedance values. On the other hand, rocks with higher porosities (5% to 10%) have lower acoustic impedance values. The inversion performed on well data also shows that the fluid bulk modulus for currently producing wells is lower than in non-productive wells, (wells with low production rates for brine and hydrocarbons), which is consistent with pore fluids containing a larger concentration

of oil.

The acoustic impedance inversion was demonstrated to be a robust technique for mapping complex structures and estimating porosities as well. However, it is not capable of differentiating different types of carbonate buildups and their origin.

To my family...

ACKNOWLEDGMENTS

I would like to thank Dr. Richard Gibson for allowing me the opportunity to work with him and to use his lab and resources. His constant guidance and advice were extremely helpful in completing my research.

I want to thank Dr. Steven Dorobek who provided all data necessary for the project as well as contact information. Thanks to Cathy Merriam for her assistance. I also want to thank Dr. Duane McVay for being part of my committee and providing his feedback.

I also appreciate the Jason Geosystems team in Houston for providing the software and for their technical support during the development of my thesis.

I cannot finish without extending my appreciation to Dr. Gibson's students: Constantinos Tzimeas, Sung Hwan Yuh, Jin Lee Kyoung, Hung Liang and Javier Perez for their help and patience.

Finally, I have to thank my family who gave me all of their support and advice to finish this project, and for helping me adapt to this new stage of my life.

TABLE OF CONTENTS

Page

CHAPTER Page

LIST OF TABLES

LIST OF FIGURES

FIGURE Page

FIGURE Page

FIGURE Page

CHAPTER I

INTRODUCTION

A quantitative, detailed description of reservoir architecture and properties is required for recovering hydrocarbons in-place. This characterization requires the integration of different data types such as well logs, core data, seismic data and other geologic information. With this information, the economics of reservoir development can be strongly improved and production enhanced.

Although well log and core data provide detailed information about the vertical variation of many of the reservoir properties, they are restricted to the vicinity of the borehole. Conversely, seismic data have lateral resolution, and not only provide information away from the wellbores, but also supply a geometric description of structural and stratigraphic aspects (Graebner and Wason, 1981).

Therefore, a method that combines high vertical and lateral resolution seems to be the most effective approach when characterizing reservoirs in two or three dimensions (Cornish and King, 1988).

Many methods have been proposed in geophysics to characterize reservoirs. One of them is seismic inversion, which essentially transforms seismic reflection data into a quantitative estimate of a rock property. As a result, this rock property describes the reservoir as much as possible.

Acoustic impedance, the product of seismic velocity and density, is an example of a rock property that is commonly used to characterize this type of reservoir. In contrast, the seismic reflection data, are generated by changes in acoustic impedance across interfaces between geologic formations. The impedance can give a more accurate and detailed structural, stratigraphic, lithologic and fluid distribution interpretation than that obtained from conventional seismic interpretation. Additionally, some production information including net pay and average porosity maps can be generated from reservoir characterization results.

Several algorithms have been developed to estimate acoustic impedance from

---

This thesis follows the style and format of Geophysics.

seismic data such as discrete recursive algorithms, that compute acoustic impedance from the reflectivity coefficients. They assume that seismic amplitudes are proportional to reflection coefficients. This method is also described as band limited, because the resulting acoustic impedance will contain the same frequency content as the input seismic data. These algorithms are fast and reliable but are unstable at high values of reflection coefficients and noise spikes. Large reflection coefficients and noise or erroneous spikes (large amplitude spikes compared to the spikes in the reflectivity series) will cause large acoustic impedance values that will give rise to instability during the inversion.

Recursive algorithms consider the seismic trace as a sequence or series of acoustic impedance. Therefore the first acoustic impedance, corresponding to the first interface, needs to be assumed to compute the second one. With the second one, the third acoustic impedance will be computed and so on. This process is done recursively until the whole series of acoustic impedance is computed. The low frequency velocity model must be estimated to generate a reliable interval velocity model which will be used to constrain the inversion (Hardage, 1987).

Continuous recursive algorithms consider that physical properties vary continuously through the earth. They are also fast and reliable algorithms but they are more stable for large reflection coefficients and noise spikes. Yet, these inversions present similar disadvantages to those of the discrete algorithms. Optimization algorithms have been also successfully applied to seismic data to estimate acoustic impedance. Generalized linear inverse methods are common but also require previous knowledge of the impedance profile. Ma (2001) used a simulated annealing optimization algorithm to invert for acoustic impedance and layer interfaces from poststack seismic data. This approach yielded the high resolution needed for reservoir characterization. In order to compute porosity distribution from estimated acoustic impedance, different approaches were also developed. For example, Madiba and McMechan (2003) computed the P and S acoustic impedance to estimate the product of the Lamé parameters (λ and μ) and density (ρ). The product $\lambda\rho$ was used to estimate porosity distributions, whereas the rigidity times density value ($\mu\rho$) was used as a gas indicator (Li and Downton, 2000).

Sparse spike methods use the seismic data to model the subsurface with a minimum number of reflection coefficients giving more reasonable geological results than recursive methods. The improvement of *Constrained Sparse Spike Inversion* (CSSI) is

that resulting impedances are required to remain within a range of values defined by the wells. One of the advantages of this method is that results are driven by seismic data, not by geologic models. Therefore, the quality of the seismic data has a great impact on results. The inversion of this method is performed by minimizing the error (between the observed and estimated data) of the reflectivity function and noise using the definitions of the l_1 and l_2 *norm* respectively. In order to constrain and reduce the non-uniqueness of the inversion, an impedance model constructed from the well log data is used.

The inverted acoustic impedance model will contain the same frequency range as the input seismic data. Another model of acoustic impedance pseudologs is generated from log data, and only the low frequency content of it is added to the former one. Thus, the final result is a broadband 3D volume of acoustic impedance pseudologs.

The data used in this study are from the Midland Basin, in Upton County, Texas (Figure 1.1). This area is part of the Permian Basin located in west Texas and southeastern New Mexico. The Midland Basin contains complex carbonate buildups in Lower Permian strata which are reservoirs in this area. These reservoirs have been producing oil since 1970 and have been extensively explored. This basin has been widely studied before as well. Tai (2001) studied the stratigraphic and structural characteristics of the southwestern Midland Basin. He also recognized the areas and the styles of the deformational processes in the basin. Merriam (1999) performed a more detailed description of the Lower Permian carbonate buildups. She described the stratigraphic units and lithofacies of the basin finding two basic types of carbonate buildups: *skeletal-sand* and *carbonate-debris*. Along with seismic and well log data she determined the depositional history of the carbonate buildups. Decalf (2001) computed several seismic attributes over the Midland Basin to recognize and image carbonate buildups. Variance and instantaneous frequency attributes were the most reliable ones to image carbonate buildups.

The data were previously used by Merriam (1999) and Decalf (2001). They were subjected to quality control to make it suitable for this study. This includes selection of specific data, complete suite of logs and generation of necessary data from pre-existing data when needed. The data comprise a 3D seismic volume acquired in the Midland Basin. The seismic data were processed to generate a zero-phase post-stacked section. A full suite of log data (including density, gamma ray, sonic and porosity logs) from wells in that area, a checkshot log to convert the data from depth

domain into time domain and seismic interpretation for two horizons are the data used for this study.

The generation of carbonate rocks has specific environmental requirements. In fact, they differ from siliciclastics in that they are generally not transported, but are organically grown and organically or geochemically precipitated. Once they are generated, they are subjected to intense diagenetic processes. These processes can radically change their original porosity and permeability in short periods of time. As a result, carbonate stratigraphy shows great variability over geologic time compared to siliciclastic stratigraphy.

Seismic velocities and densities in carbonates rocks are significantly larger than in siliciclastic rocks. Therefore, for a comparable siliciclastic stratum, a carbonate stratum will have lower spatial and vertical resolution due to its high velocity and density values. Diagenetic processes can also deteriorate the propagation of seismic waves. In some cases, these features generate back-scatter and convert surface waves to compressional and shear waves. In more complex areas, where carbonates are mixed with other lithologies, significant problems can be observed such as statics, imaging and resolution problems, and even the best seismic processing algorithms can not solve the resulting problems (Palaz and Marfurt, 1997).

As previously mentioned, mapping carbonate reservoirs in common seismic sections is a difficult task. Carbonate buildups are imaged as mounded and draped reflections, the edges of buildups are generally marked by stratal onlap or by sudden changes in internal layering, and seismic facies transitions are highly variable. Since the acoustic impedance data provide superior information about lithology and stratigraphy, and produce a section with more temporal and spatial resolution, the acoustic impedance inversion (CSSI) is proposed here as an efficient tool to image, locate and characterize these complex structures. Additionally, new locations of carbonate buildups are identified during this study as prospective drilling targets. With the aid of well log data, a volume of porosities is generated from the broadband inverted acoustic impedance model. This volume of porosities is corroborated from known porosities on carbonate buildups, and an estimate of porosities for new prospective areas is computed as well.

In order to predict and validate previous results, theoretical analyses to estimate acoustic impedance were also performed. They include the Time-Average equation and Gassmann equation. These theoretical models help to describe and characterize

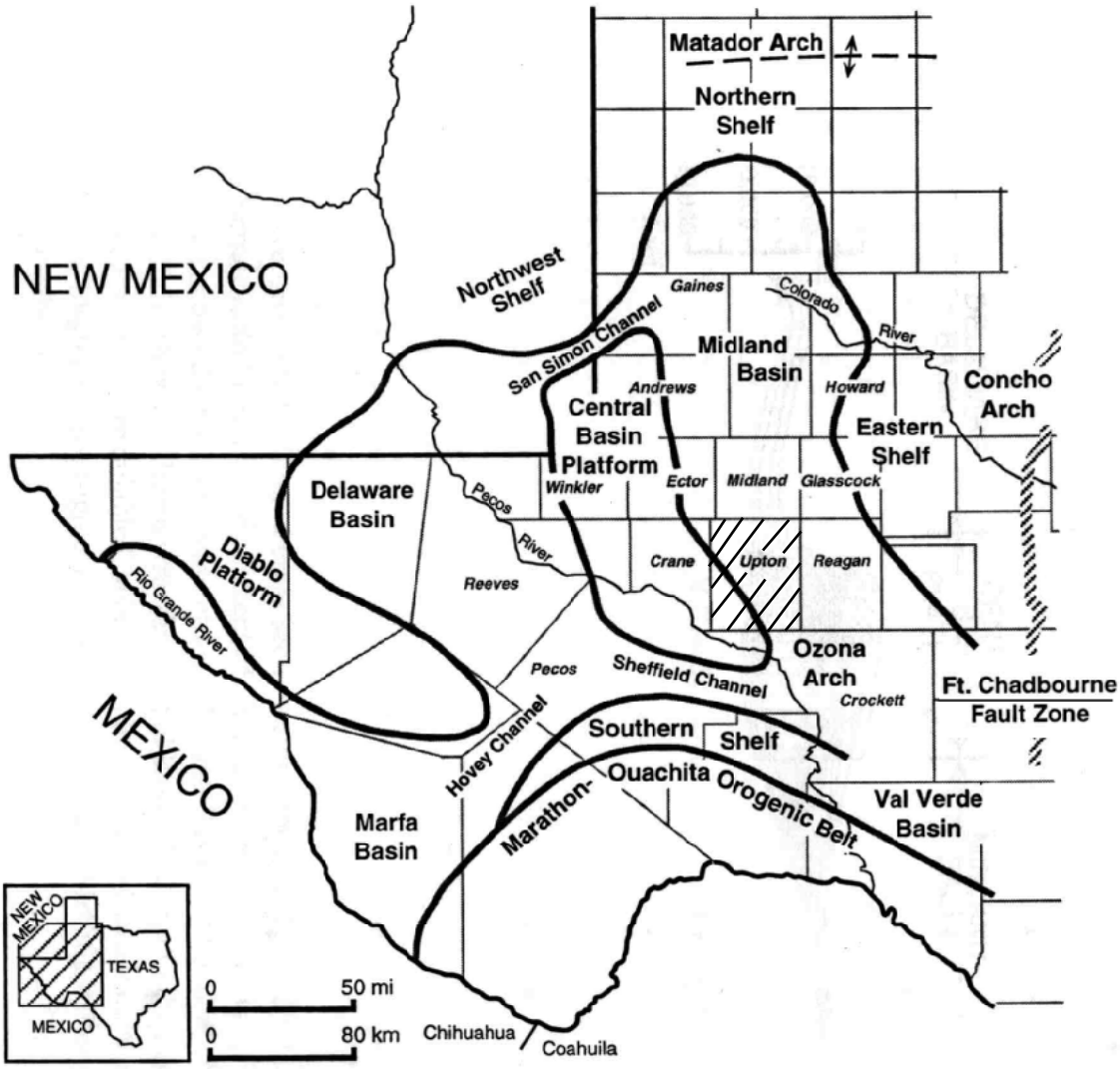

Fig. 1.1. Location of the Permian Basin. Modified from McCunn and Walker (1962) and Yang and Dorobek (1995b) *in* Merriam (1999).

physical properties of carbonate buildups. Therefore, variations in acoustic impedance will be explained in terms of distributions of physical properties such as porosity, mineral content, density and fluid fillings. The Time-Average equation relates the compressional velocity in fluid saturated rocks to those in the solid rock matrix and pore fluid. The Gassmann equation relates the moduli of the fluid saturated porous medium to those of the frame, grains and pore fluid. Biot's theory is also used to calculate velocities in fluid saturated rocks. This theory is used at higher frequencies where the Gassmann equation is not valid. None of these models take into account the pore geometry. Other models, such as Kuster-Toksöz, consider information about pore geometry when computing compressional velocity in porous rocks (Wang et al., 1991).

This thesis is organized as follows: In the first chapter an introduction about the generalities of the methodology and objectives are presented. The second chapter depicts a geological description of the area as well as seismic characteristics of the carbonate buildups and the reservoir. The third chapter explains the theory of recovery of the acoustic impedance and the inversion applied in this study. The fourth chapter presents the methodology followed to perform the inversion, and finally the fifth chapter shows the results achieved during the inversion, the theoretical approaches to predict observed data and a discussion of them.

CHAPTER II

REGIONAL GEOLOGY OF THE PERMIAN BASIN

The Permian Basin of west Texas and southeastern New Mexico covers a wide area of sub-basins. The area of interest in this study is the southeastern portion of the Midland Basin located in Upton County, Texas (Figure 1.1).

The Permian Basin is located in the foreland of the Marathon-Ouachita orogenic belt and is composed of a complex structure of sub-basins surrounded or separated by fault-bounded uplifts. The complexity of the basin occurs as a result of diverse structural styles, subsidence histories and different geometries of sub-basins and uplifted areas (Yang and Dorobek, 1995a).

2.1 Location and structural boundaries

The Midland Basin is separated from the Delaware Basin to the west by the Central Basin Platform. This feature is a prominent intraforeland uplift characterized by several *en echelon* fault-bounded structures. To the east, the Midland Basin is bounded by a complex series of north-south trending fault segments called the Fort Chadbourne Fault Zone. This fault zone separates the Midland Basin from the Eastern Shelf. The Ozona Arch is an eastern extension of the Central Basin Platform that separates the southern part of the Midland Basin from the Val Verde Basin (Yang and Dorobek, 1995b). The northern boundary of the Ozona arch is defined by the Big Lake Fault zone. A southward-dipping homocline separates the Midland Basin from the Northern Shelf (Tai, 2001) (Figure 2.1).

The current structural features present in the Permian Basin have not been subjected to significant deformation since late Paleozoic time, except for minor tilting along its margins (Yang and Dorobek, 1995b). Prior to the late Paleozoic deformation, the present Permian Basin was occupied by the Tobosa Basin, a shallow semi-circular intra-continental basin that probably formed during an extensional event in late Precambrian to early Cambrian time. Gradual subsidence occurred in the Tobosa Basin from early Cambrian to middle Mississippian time.

The antecedent Tobosa Basin consists of shallow carbonate facies interbeded with

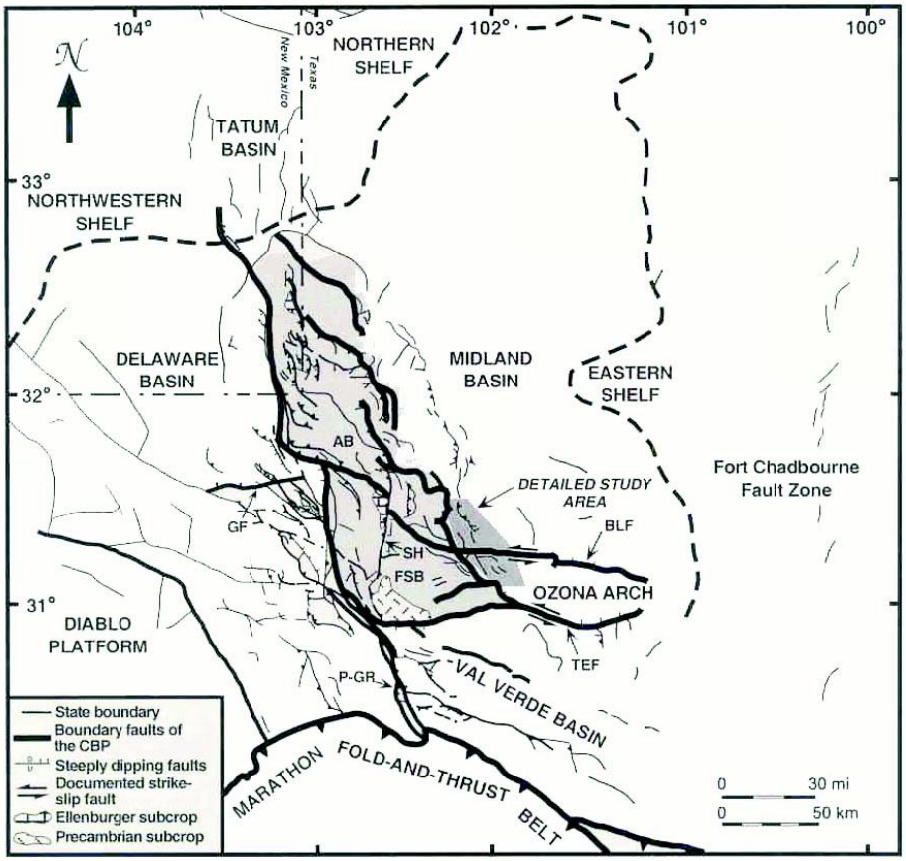

Fig. 2.1. Generalized fault map of the Permian Basin. Shaded areas represents study area covered by Chevron. Modified from Yang and Dorobek (1995b) *in* Tai (2001). AB=Andector Block, FSB=Fort Stockton Block, BLF=Big Lake Fault, GF=Grisham Fault, P-GR=Puckett-Grey Ranch Fault Zone, SH=Sand Hills Fault, TEF= Todd Elkhorn Fault.

thin shales. The deposition of these shallow facies continued until late Mississippian time when an oblique convergence between Laurasia and Gondwanaland occurred generating the Marathon Ouachita orogenic belt. Due to the orogenic progress, the former Tobosa Basin was differentiated into crustal uplifts and sub-basins that now characterize the Permian Basin (Yang and Dorobek, 1995a). One of the most important uplifts generated during Pennsylvanian to early Permian time is the Central Basin Platform, a prominent fault-bounded paleotopographic high that separates the Midland Basin and Delaware Basin. During middle Pennsylvanian to Early Permian time, the orogenic belt moved northward to its present location, and the present Val Verde Basin was the foredeep to the orogen.

The Val Verde, Midland and Delaware Basins were subjected to two majors phases of deformation during Pennsylvanian to Early Permian time. The tectonic history of these basins was apparently affected much more by uplift of the Central Basin Platform than by the encroaching Marathon orogenic belt.

Shallow-water carbonate facies of the Strawn limestone that overlie the pre-Desmoinesian unconformity maintain constant thickness across the Val Verde Basin. The Strawn carbonate strata probably were deposited on a ramp that extended across all of the the non-overthrusted parts of the Val Verde Basin (Yang and Dorobek, 1995b). Thickness of the middle Pennsylvanian Strawn limestone is relatively constant over the Midland and Val Verde Basins. However, the Strawn Limestone thickens in the center of Delaware Basin. Additionally, strata that overlie the Strawn limestone in the Midland Basin thicken away from the Central Basin Platform. This feature suggests that the subsidence pattern in the Midland Basin changed dramatically near the end of the middle Pennsylvanian time. Upper Pennsylvanian through Wolfcampian strata in the Val Verde Basin thicken dramatically toward the Marathon orogenic belt, whereas the Strawn limestone remains relatively constant in thickness from the southern part of the basin to the Ozona Arch. These thickness trends indicate that subsidence in the Val Verde Basin also changed dramatically near the end of middle Pennsylvanian time. These regional variations in stratigraphic thickness indicate that while initial deformation in the Marathon-Ouachita orogenic belt began in Mississippian time, major subsidence in the Midland, Delaware and Val Verde basins did not start until after middle Pennsylvanian time (Yang and Dorobek, 1995b).

Lithofacies variations in Middle to Upper Pennsylvanian strata across the Midland, Delaware, and Val Verde basins provide additional evidence for differential

subsidence in these basins. During middle Pennsylvanian time, the Strawn limestone was deposited as a thin continuous interval of carbonate strata over the Midland and Val Verde Basins. Upper Pennsylvanian strata through the Permian Basin region are characterized by rapid lateral facies changes from shallow carbonate platform facies on top of paleotopographic highs to deep water shale facies in adjacent basins. Clearly, these facies changes suggest that important differential subsidence began in all basins during the late Pennsylvanian. Gradual subsidence occurred across the entire Tobosa Basin from early Paleozoic to early Pennsylvanian time. During middle to late Pennsylvanian time a major subsidence occurred in all three basins (Midland, Val Verde and Delaware Basins).

Yang and Dorobek (1995a) have shown that the Val Verde, Midland and Delaware basins were affected by combined tectonic loads of the Marathon orogenic belt, Central Basin Platform, Diablo Platform and inferred structures on the eastern side of the Midland Basin. In addition, late Paleozoic basin geometries from the Permian Basin are affected by lateral variations in lithospheric ridigity across the Marathon-Ouachita foreland. Yang and Dorobek (1995a) showed that some foreland basins are extremely complex and may be influenced by the combined effects of several topographic loads.

An accurate end of synorogenic deposition across the Permian Basin is difficult to determine. Fault terminations and stratigraphic intervals provide few constraints to identify the end of tectonic activity in the Marathon-Ouachita foreland. Upper Wolfcampian strata unconformably overlie thrust sheets along the leading edge of the orogenic belt, indicating that shortening in the Marathon orogenic belt to the south of the Val Verde Basin ceased by the end of early Wolfcampian time. Well logs correlated across the Val Verde Basin demonstrated that thickening of upper Wolfcampian strata toward the Marathon orogenic belt reflects the greater amounts of flexural subsidence in the Val Verde Basin caused by the orogenic belt. The Lower Spayberry Formation and correlative strata that overlie upper Wolfcampian strata are relatively uniform in thickness, with lithofacies that do not vary much across the Val Verde Basin. These relationships suggest that subsidence due to flexural loading by Marathon orogenic belt ceased after Wolfcampian time, and later regional subsidence in the Val Verde Basin was more uniform. In conclusion, the evidence stated suggests that the interval of rapid subsidence slowed considerably at the end of Wolfcampian time but continued until the end of Permian time (Yang and Dorobek, 1995b).

2.2 Stratigraphy of Midland Basin

The upper Pennsylvanian to Wolfcampian strata along east-west basin profiles through the Midland Basin are thinner with no pronounced changes in thickness. Lower Paleozoic to middle Pennsylvanian strata are thickest immediately adjacent to the Central Basin Platform and thin eastward toward the Eastern Shelf. Lithofacies within these stratigraphic units are also relatively uniform. The overlying upper Pennsylvanian to Wolfcampian strata are thickest in the northeastern part of the basin.

Shallow water carbonates lithofacies of the middle Pennsylvanian Strawn limestone extend across most of the Midland Basin and have relatively constant thickness. Lithofacies in upper Pennsylvanian to Wolfcampian strata change dramatically near the eastern and western edges of the Midland Basin. Upper Pennsylvanian to Wolfcampian strata on both sides of the Midland Basin consist of carbonate platform facies that change basinward into fine grained siliciclastic facies. In the center of the basin, thick, upper Pennsylvanian shales overlie shallow water carbonates of the Strawn Limestones. Upper Pennsylvanian to Wolfcampian carbonate strata are thicker in the center of the basin than near the eastern side of the Midland Basin (Yang and Dorobek, 1995b).

2.3 Wolfcampian - Leonardian Buildups

Wilson (1975) gives a general definition of a carbonate buildup as a locally formed and laterally restricted body of carbonate sediment which possesses topographic relief. This definition contains no information about internal facies composition since they vary upon the place of formation, however it is useful as a general concept of the buildup.

Using cores and well logs from Wolfcampian - Leonardian buildups trends in the south-west Midland Basin, Merriam (1999) showed that there are two types of carbonate buildups. *Skeletal-sand buildups* consist largely of layered to massive skeletal grainstone to packstone beds and *carbonate debris buildups* consist of lithoclastic debris that was derived both locally from adjacent skeletal sand buildups and from updip shallow-water carbonate platform areas.

2.3.1 Location of the buildups in the Midland Basin

The carbonate buildups in the south west Midland Basin have low relief and complex internal lithologies, which make it difficult to identify them on seismic sections. Decalf (2001) computed various seismic attributes in order to obtain a clearer image of the carbonate buildups and determine their location. The variance attribute gives reliable results for skeletal-sand buildups, but was less useful for identifying carbonate-debris buildups. This probably is true because carbonate debris buildups are composed of sediment-gravity flow deposits, skeletal sand buildups, which are probably more lithologically homogeneous and other ramp facies, rather than hydrodynamically constructed features. Merriam (1999) suggested that skeletal sand buildups are associated with paleobathymetric lows on top of the Strawn Formation, whereas carbonate debris buildups formed on paleobathymetric highs.

The variance attribute allows the identification of three skeletal sand buildups in the northwestern part of the Amacker survey and one in the southeastern part of it. This study confirms previous results reported by Merriam (1999).

2.3.2 Dimension of the buildups

Carbonates buildups in Midland Basin vary regionally in thickness and width. Merriam (1999) used well data and seismic sections to show that buildup width ranges from 762-915 m (2500-300 ft) and thicknesses vary from 84-267 m (277-877 ft).

In the Amacker 3D survey, Merriam (1999) reported that the top of the carbonate buildups is between 2607 and 2714 m (8550 to 8902 ft) depth, while the base of the carbonate ranges from 2816 to 2895 m (9238 to 9495 ft) depth. On average, the skeletal-sand buildups are 195 m (640 ft) thick and carbonate-debris buildups are 170 m (558 ft) thick.

2.3.3 Buildup lithofacies

The Wolfcampian - Leonardian carbonates buildups are characterized by a wide variety of lithofacies that make it difficult to establish a stratigraphic framework. In spite of the relative abundance of lithofacies from one buildup to the next, each lithofacies can be found in nearly every seismically identified buildup.

According to Merriam (1999) facies present in the Wolfcampian - Leonardian

carbonates buildups include: *"dark colored shale facies, lithoclastic facies, grain-supported facies, matrix supported facies and boundstone facies"*.

Dark colored shale facies consist of dark-colored shale with skeletal limestones fragments, minor radiolarians, light-colored mud clasts and shale stringers and variable amounts of diagenetic detrital grains. This facies has thin to thick horizontal to subhorizontal interbeds of shallow water skeletal grainstone to wackestone/lime mudstone. Dark colored shale is interpreted as a basinal, deep-water and sub-wave base facies.

Lithoclastic facies are mainly composed of moderately to poorly sorted, thick lithoclastic-rich beds. Lithoclasts consist of shallow-water skeletal grainstone, packstone, wackestone, lime mudstone and boundstone, with less common of light-colored shale, dolomite and argillaceous dolomite. Lithoclastic facies are found in carbonate-debris buildups and comprise 28% $\sim$ 58% of those buildups. They were derived from shallow-water carbonate platform areas located on the Central Basin Platform, the Ozona Arch, and locally from adjacent skeletal-sand buildups.

Grain-supported facies are composed of skeletal grainstone to packstone lithologies, including peloidal grainstone and some shallow-water lithoclasts. This lithofacies is gray to dark brown in color. These facies are found mostly in skeletal-sand buildups as individual beds and comprise 69% of these. This facies is interpreted as *in situ* shallow-water deposits that formed within or just below wave base. The interpretation is supported by evidence that suggest deposition within the photic zone and under aerobic conditions as indicated by grain-supported fabrics, extensive bioturbation and abundant shallow-water grains types.

Matrix-supported facies consist of skeletal wackestone to lime mudstone. The color of this facies ranges from gray to dark brown. Grain types include micritic-composite-coated grains and whole fossils to abraded fragments of crinoids, phylloid algae and ostracodes. Matrix-supported facies are found mostly in skeletal-sand buildups where it comprises about 16% of the skeletal-sand buildups. This facies is also found in the carbonate-debris buildups as discrete layers. Matrix-supported facies are interpreted as *in situ* deposits formed below wave base and within the photic zone.

Boundstone facies are rare in the buildups from the southwest Midland Basin. Boundstone facies contain large phylloid algae, bryozoans and brachiopods within an argillaceous lime mudstone matrix. The contacts between boundstone facies and

other buildups facies are sharp but no erosional. Lithoclasts of boundstone are common in lithoclastic facies. The rare occurrence of *in situ* boundstone facies within Wolfcampian-Leonardian buildups suggests that most boundstones lithoclasts were probably sourced from updip platform-margin facies belts.

2.3.4 Internal stratigraphy of buildups

As previously mentioned, lithofacies in carbonate buildups are variable, therefore they show an incoherent internal seismic reflectors. It still is possible to develop an internal stratigraphic framework based on integration of cores, well logs, biostratigraphic data, seismic data and published third-order sea level curves (Merriam, 1999). A depositional model can be established if an internal stratigraphic framework is proposed. Figure 2.2 shows a generalized stratigraphic column for the Permian Basin.

Merriam (1999) established four correlatable units. The first stratigraphic unit corresponds to the Eddleman formation. It consists of shallow-water skeletal grainstone/packstone to skeletal packstone/wackestone facies. This interval conformably overlies the Wolfcamp shale interval and can be correlated in both types of buildups.

The second stratigraphic unit is the Twenty-one formation that can be correlated throughout the study area. This formation is composed of dark-colored calcareous shale with interbeded limestone. The Twenty-one formation has conformable contacts with underlying and overlying carbonate facies in some skeletal-sand buildups. In other buildups, the Twenty-one formation is formed below the base of the first carbonate interval.

The third stratigraphic unit in the Amacker formation, which conformably overlies the Twenty-one formation can be correlated through the buildup trend. This formation largely consists of shallow-water skeletal grainstone to wackestone, lime mudstone, minor algae boundstone and lithoclastic facies.

The fourth stratigraphic unit is the Tippet shale, which can be correlated throughout the study area. This formation conformably overlies the Amacker formation and represents termination of the buildups growth. The Tippet shale mainly consists of dark-calcareous shale facies.

2.3.5 Seismic features of carbonate buildups

Commonly carbonate buildups generate strong reflections in seismic data due

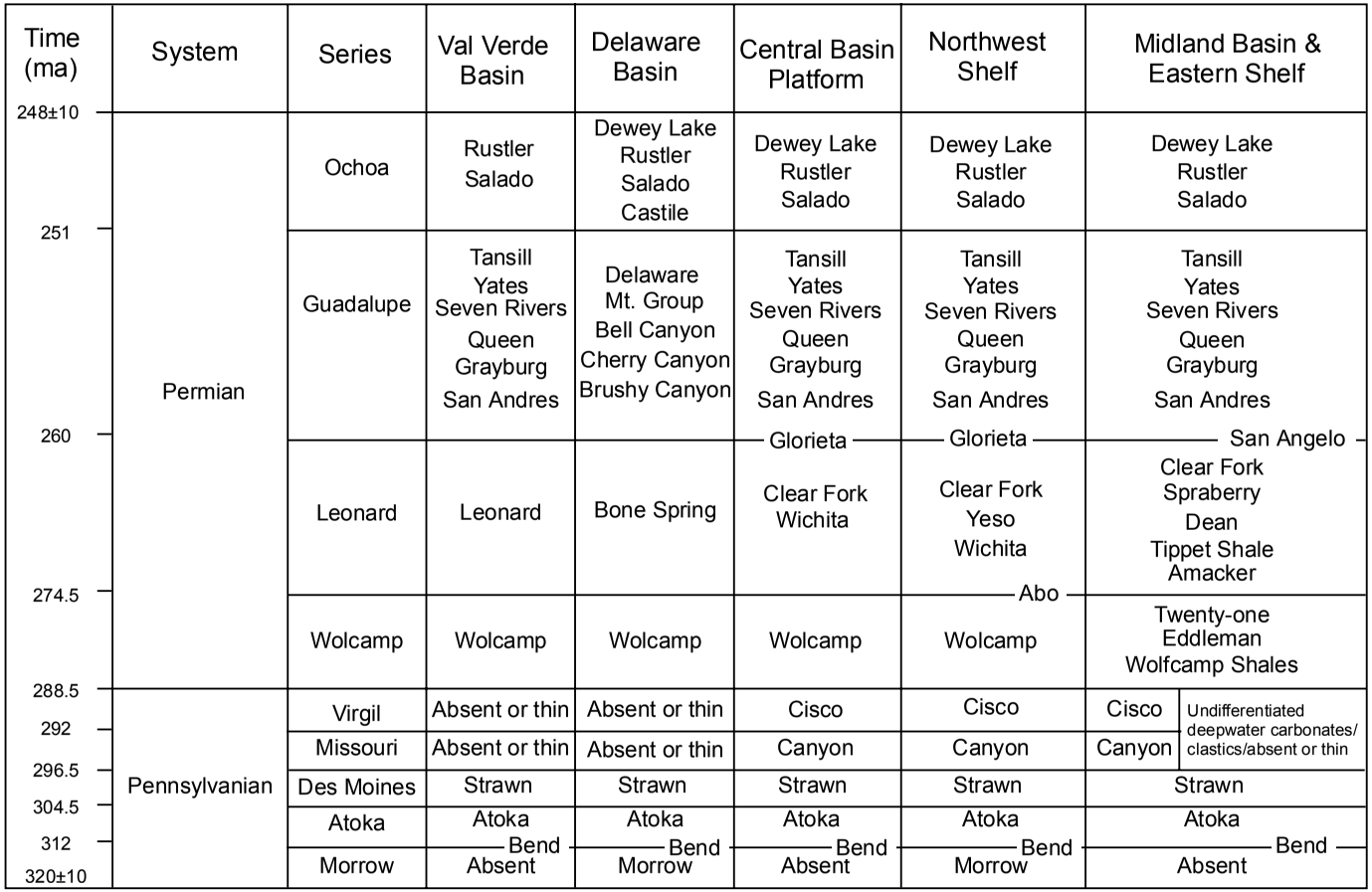

Fig. 2.2. Stratigraphic correlation chart for Pennsylvanian and Permian strata across the Permian Basin. Modified from (Merriam, 1999).

to the velocity contrast between carbonates and the surrounding strata. However, some problems occur when carbonate strata are mixed with shale and sandstone; the seismic data may or may not reflect strong horizons due to poor contrast of the acoustic impedance between strata. Individual buildups may also show pull-up effects on underlying reflections because the velocity of surrounding strata is typically lower than the velocity of the carbonate buildup (Decalf, 2001).

Seven stratigraphic horizons were mapped by Merriam (1999) using digital well-log data, check-shot surveys and synthetic seismograms. These include: the Strawn limestone, top and base of Wolfcampian-Leonardian carbonate, top of the Tippet shale, top of the Dean sandstone, top of the Clearfork and top of the Yates formation. In this study, only the Tippet shale and the Strawn Limestone were used. The Strawn limestone and the top and bottom of the carbonate are difficult to follow through the area due to lateral thickness variation, tuning effects and structural complications. The Tippet shale appears as a strong reflector throughout the study area.

Seismic data show that carbonate debris buildups have continuous reflections and no compactational drape in overlying strata. In addition, gamma-ray logs show shaly response through these buildups. On the other hand, skeletal-sand carbonate buildups appear as mounded features with chaotic to laterally discontinuous internal seismic reflectors and have cleaner gamma-ray log response (Decalf, 2001). Cleaner carbonate buildups are nearly seismically transparent, whereas more argillaceous and lithologically heterogeneous strata have stronger internal reflections (Merriam, 1999).

The Amacker and Eddleman formations which include the carbonate buildups are parallel to subparallel layers deposited on top of parallel to subparallel strata of middle to upper Pennsylvanian age. Those reflectors in seismic data follow the structural pattern of the underlying strata. The carbonate buildups can be recognized on seismic sections by the high-amplitude reflector of the Tippet shale above the buildup (Merriam, 1999).

2.4 Reservoir characteristics

The complex facies and stratal relationships within carbonates buildups as well as their complex diagenetic history make these reservoir heterogeneous and difficult to predict in the subsurface. The Wolfcampian-Leonardian carbonate buildups in the southwestern Midland Basin have low permeability and matrix porosity values

($\approx$ 5%) (Merriam, 1999). Porosity is enhanced by extensive fracturing and grain dissolution creating intergranular, intragranular and moldic porosity. In addition, permeability is also increased by fractures connecting separated carbonate buildups. However, the productive formation in the skeletal-sand and carbonate-debris buildups are the Amacker and Eddleman formation with the largest reserves found in cleaner carbonate buildups (Merriam, 1999). Table 2.1 shows additional information of the production of the different carbonate buildups found in Amacker survey. Figure 2.3 shows the cumulative oil production for wells in Amacker survey. Notice that wells that have perforated skeletal sand buildups (SS) are more productive than those that have penetrated carbonate debris buildups (CD). In this study, the term "productive well" refers to wells that are currently producing economic quantities of oil, gas or brine. In contrast, the "non-productive wells" are those wells that had low rates of production of brine and hydrocarbons and were therefore abandoned and were considered dry (personal communication, Nancy Moore. 2003).

Table 2.1. Production of wells in the Amacker survey and associated carbonate buildups. The size of the bullets represents the relative production volume of the products.

Well	Oil	Gas	Brine	Dry	Type of Buildup
Amk_6404	●	●			Skeletal Sand
Amk_64_2	●	●	•		Carbonate Debris
Amk_64_3	●	●			Skeletal Sand
Amk_1A				●	Carbonate Debris
BHP_2F	●	●			Skeletal Sand
Eddm_6	●	●	•		Carbonate Debris
Eddm_7	●	●	●		Carbonate Debris
Eddm_8	●	●	•		Skeletal Sand
Hunt_77_6				●	Skeletal Sand
Hunt_77_5	●	●	•		Skeletal Sand
Hunt_78_G_3	●	●			Skeletal Sand

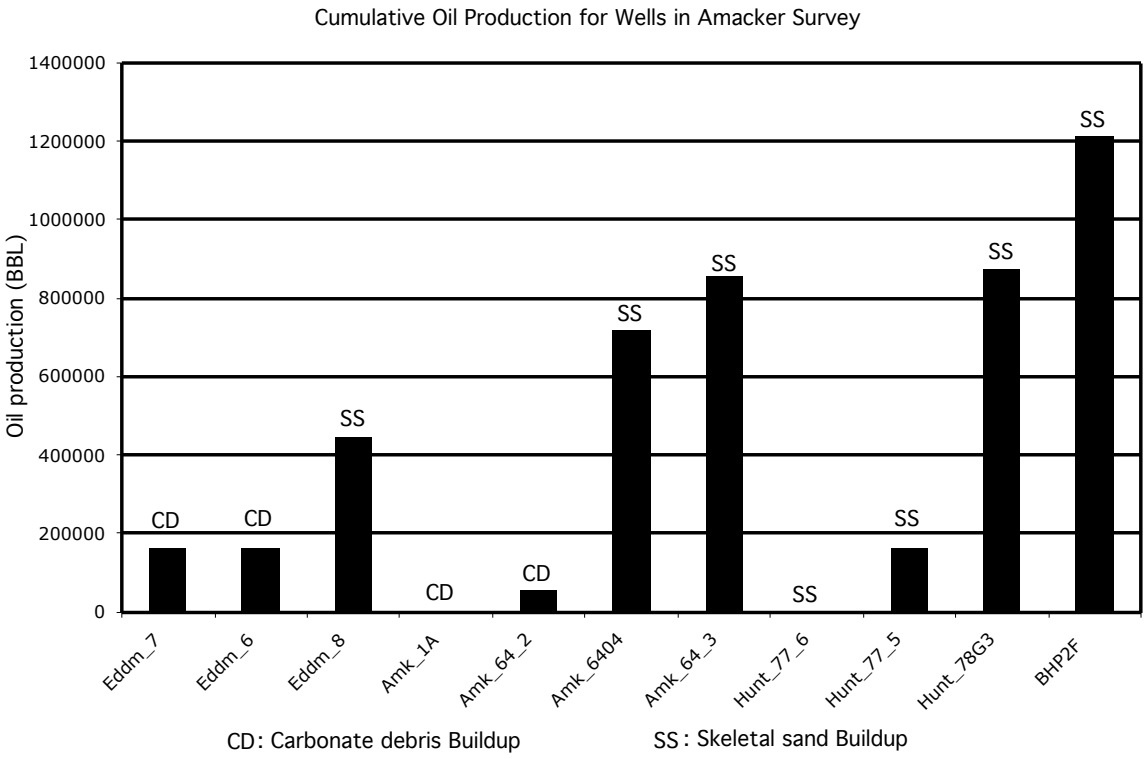

Fig. 2.3. Cumulative oil production for wells in Amacker survey. SS refers to wells that have perforated skeletal sand buildups, whereas CD refers to wells that have perforated carbonate debris buildups.

CHAPTER III

BASIC THEORY

One of the main purposes in reflection seismology is to recover the acoustic impedance as a function of depth from the normal incidence seismograms. It is widely accepted that the acoustic impedance is the product of the seismic velocity (v) and density (ρ). Thus, an acoustic impedance inversion is the transformation of seismic data into pseudoacoustic logs at every trace.

Seismic amplitudes are layer interface properties that reflect relative changes in acoustic impedance. They are used for more specific achievements such as an indicator of reservoir structures and delineating hydrocarbon zones. In addition, when correlated with well log data, the accuracy is improved and it helps to determine changes in facies far from wells (Becquey et al., 1979). Conversely, acoustic impedance pseudologs are rock properties that can provide information about lateral changes in lithology as well as basic characteristics of the rocks, including porosity and pore fill.

It is important to recall the difference between acoustic impedance and elastic impedance. The former is applied to poststack or zero-offset sections, while the latter is a generalization of the acoustic impedance for variable incidence angles or nonzero-offset sections. Essentially, elastic impedance is an approximation obtained as a linearization of the *Zoeppritz* equations; it is a function of P-wave velocity, S-wave velocity, density and angle of incidence.

When converting seismic amplitudes into acoustic impedance pseudologs the lack of low and high frequencies in seismic data is also present in the impedance model. This problem can be clearly seen from the convolutional model

$$x(t) = r(t) * w(t), \tag{3.1}$$

where $x(t)$ is the seismogram, $r(t)$ is the reflectivity function, $w(t)$ is the seismic wavelet and $*$ represents the convolutional operator. Generally, $r(t)$ is broadband, but the seismic wavelet is band-limited, commonly between $10 \sim 50$ Hz. As expected, when the convolution is applied, the seismogram is band-limited as well (Figure 3.1). As a result, information about $r(t)$ outside this band is not easily recoverable from

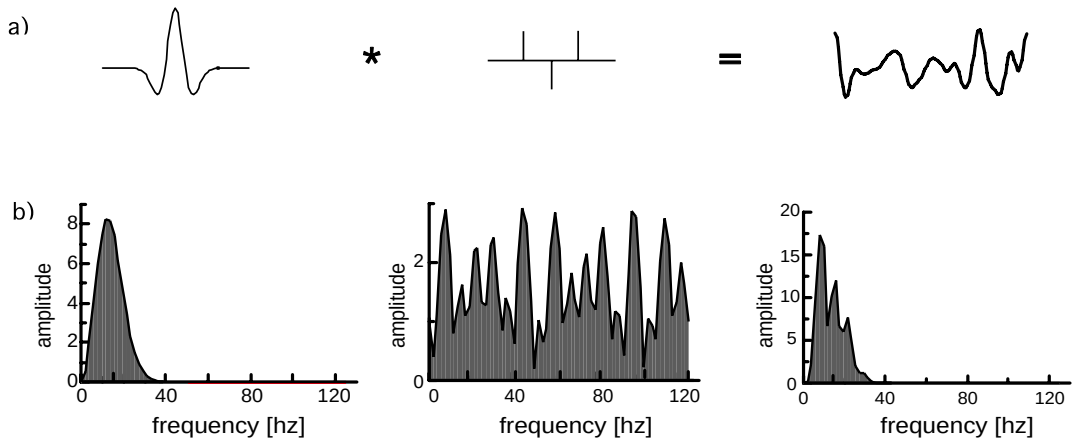

Fig. 3.1. Schematic representation of the convolutional model. (a) Convolutional model in time of the wavelet with the reflectivity series and its corresponding seismogram. (b) Amplitude spectra of the wavelet, reflectivity and seismogram.

seismograms, and thus acoustic impedance is band-limited. This implies that low and high frequencies are missing (Oldenburg et al., 1983).

In order to improve the resolution of the band-limited acoustic impedance model, low frequencies need to be added. This information can be extracted from reflection-moveout velocity information, log data, or time migration velocities. Once this information is included, improvements are applied to the seismic data such as tuning effects, ability to identify gradational coarsening upward sequences, and the ability to resolve accurately thin beds. Overall, an acoustic impedance model contains all the information from seismic data and well-log data without problems caused by wavelets such as side lobes.

3.1 Acoustic impedance

Synthetic velocity logs are of great importance for seismic stratigraphy. They are obtained during the inversion of reflection seismograms. The acoustic impedance logs and the reflection coefficients are key quantities when obtaining synthetic velocity logs. As stated, acoustic impedance is the product of the density (ρ) and velocity (v), whereas the reflection coefficient is the fraction of incident amplitude that is reflected from an acoustic impedance change. The reflection coefficient is generally expressed as

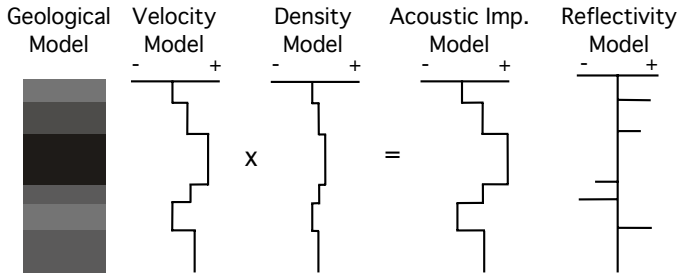

Fig. 3.2. Schematic representation of the reflectivity series generated from changes in acoustic impedance.

$$r(t) = \frac{\xi_{t_2} - \xi_{t_1}}{\xi_{t_2} + \xi_{t_1}}, \tag{3.2}$$

where t is the two way time, ξ_{t_1} is the acoustic impedance of the overlying layer, and ξ_{t_2} is the acoustic impedance of the underlying layer.

The equation 3.2 can be either negative or positive. If a positive value is obtained, this can be considered due to an increase in the acoustic impedance between layers, whereas a negative value is obtained if a decrease in the acoustic impedance occurs. Reflection coefficients can vary between +1.0 and -1.0. This variation depends upon the magnitude of the acoustic impedance, which varies with changes in velocities and densities (Figure 3.2). Large velocity differences produce large reflection coefficients. However, variations in density can contribute to changes of the reflection coefficient but are less pronounced (Hardage, 1987).

In a sedimentary sequence of rocks, reflection coefficients are generated at each interface as the acoustic impedance changes. These boundaries in a seismogram are called reflectors. Hence, they are visible only if there is an acoustic impedance change, and are large enough to be recorded by seismometers. Acoustic impedance has been studied in enough detail that it is possible to relate the amplitude of the reflection to the size of the acoustic impedance change and therefore determine the origin of the reflection (Badley, 1985). Some rock configurations produce typical reflections in seismograms. These predictable responses have led geoscientists to recognize them systematically. For example, changes in acoustic impedance between water-filled sands, gas-filled sands, and shales are large and produce strong reflections. However, sometimes there is no acoustic impedance contrast between a reservoir sandstone and a claystone seal, making reflections difficult to recognize. There are cases where

a reservoir of massive sands interbeded with shales shows no internal reflections, whereas gas filled reservoirs can show them (Badley, 1985).

3.1.1 Recovery of acoustic impedance

Many algorithms have been developed to estimate acoustic impedance from seismic data. The most common velocity inversion algorithm are the ones that predict impedance profiles based on recursive methods. Algorithms based on a generalized linear inversion methods are common as well. Other approaches less widespread are auto-regressive algorithms and non-linear inversions.

On the whole, algorithms that invert velocity logs have to take into account some considerations. The earth consists of planar, parallel and homogeneous impedance layers; any complexity introduced during the inversion is considered an anomaly. The inversion also assumes that the convolution contains no noise, as expressed in equation 3.1. In addition, for all 1-D velocity inversions, the common midpoint (CMP) data assumes that the reflectivity series of the earth immediately below the CMP is directly proportional to the successive amplitude values of the final stacked section seismic trace at the CMP location (Hardage, 1987).

The discrete recursive algorithm consists of the inversion of the equation 3.2 into the form

$$\xi(t_{n+1}) = \xi(t_n)\left(\frac{1+r(t_n)}{1-r(t_n)}\right). \tag{3.3}$$

This inversion is the most common, as it is a fast and reliable algorithm. However, occasional difficulties arise during the inversion. These include the estimation of an initial impedance $\xi(t_0)$, the estimation of the low frequency velocity model, the normalization of the inverted trace, the difficulty of preserving the exact impedance values and impedance boundaries during the inversion and, the instability of the solution in the presence of large values of reflection coefficients and noise spikes (Hardage, 1987).

On the other hand, the continuous recursive algorithm considers that the earth now consists of a medium with the physical properties of velocity and density varying continuously, rather than a medium with homogeneous layers with definite boundaries. Additionally, this inversion is a fast algorithm and gives reliable estimation of theoretical values. In contrast to the discrete recursive method, it shows more stabil-

ity in the presence of large reflection coefficients and noise spikes. Yet, this inversion presents similar problems to those of the discrete algorithm. Once more, the initial acoustic impedance must be estimated, and can be troublesome if the near surface is exposed to severe weathered conditions. Moreover, the inversion cannot be started at any nonzero time along the trace, the low frequency velocity model must be assumed, the inverted trace must be normalized to know reflection coefficients, precise values of impedance and impedance boundaries are difficult to preserve, estimated velocities are not exact for extremely large reflection coefficient values and there is a progressive introduction of velocity errors due to the approximations (Hardage, 1987).

Generalized linear inverse methods have also become commercially important. These methods require previous knowledge of the impedance profile, and therefore an initial input of the impedance profile as well as the observed seismic trace at the same spatial location. A forward model is generated using the initial impedance information and a wavelet similar to the one contained in the observed trace data. The forward model and the observed trace are compared and differences are evaluated. The synthetic trace is then slightly perturbated until the difference between the observed trace and the modeled trace reaches a minimum.

This method requires the same assumptions as preceding ones. In contrast, the exact impedance value and boundary positions can be preserved and non-reflectivity information such as intra-bed multiples, dispersion, and absorption can be included in the observed trace. The inclusion of these propagation effects make the inversion more expensive. However, other advantages include the facts that the solution is insensitive to errors in the assumed source wavelet, the seismic to impedance scaling factor can be independently obtained and the forward model can be modified as necessary in order to describe the effects of the earth, the data acquisition and processing. Equally notable are the disadvantages, namely, the algorithm is unstable in the presence of high noise, and the solution is non-unique and relatively expensive in terms of computing time. The fact that the initial impedance boundaries, impedance contrasts and intra-formation impedance gradient are known, give the possibility to obtain exact and/or highly reliable results (Hardage, 1987).

Many authors have developed different approaches to estimate synthetic acoustic impedance from seismic data. Some of the works presented here are of particular importance when the seismic data is both broadband and band-limited.

3.1.2 Estimation of acoustic impedance from broadband seismic data

In order to recover the acoustic impedance from reflection seismograms, Oldenburg et al. (1983) assumes in his model that the earth is composed of parallel layers with constant physical properties (ρ, v, ξ). Additionally, the source energy propagated through the earth is reflected back toward the surface at each layer boundary. Geometrical divergence, anelastic absorption, dispersion of the wavelet, transmission losses across the boundaries and multiple reflections are neglected here to simplify the computation. The observed seismogram $x(t)$ is recorded as a function of time and expressed as in equation 3.1.

The reflectivity function can be written as

$$r(t) = \sum_{k=1}^{NL} r_k \delta(t - t_k), \tag{3.4}$$

where $r(t)$ is non-zero for those two-way traveltimes t_k from the k^{th} layers. NL represents the number of layers and r_k is the reflectivity coefficient at the interface between the k^{th} and $(k+1)^{th}$ layer. The acoustic impedance can be written as

$$\xi_k = \rho_k v_k, \tag{3.5}$$

where ρ_k and v_k are the density and the velocity of the k^{th} layer respectively.

The reflectivity coefficient at the k^{th} layer is expressed as

$$r_k = \frac{\xi_{k+1} - \xi_k}{\xi_{k+1} + \xi_k}. \tag{3.6}$$

Equation 3.7 represents the acoustic impedance as function of the reflectivity coefficients

$$\xi_{k+1} = \xi_k \left(\frac{1 + r_k}{1 - r_k} \right) = \xi_1 \prod_{j=1}^{k} \left(\frac{1 + r_j}{1 - r_j} \right). \tag{3.7}$$

From equations 3.1 and 3.7 the acoustic impedance from seismograms can be calculated. In order to estimate it, an inverse filter should be found such that

$$w(t) * v(t) = \delta(t), \tag{3.8}$$

then, convolving $v(t)$ with $x(t)$ in 3.1 gives

$$r(t) = x(t) * v(t). \tag{3.9}$$

If the earth is assumed to be layered, $r(t)$ will have the form given in equation 3.4, and therefore the coefficients r_k can be estimated. Finally, equation 3.7 allows us to determine the acoustic impedance for any layer. Since the wavelet is band-limited, it is impossible to find a filter $v(t)$ that obeys equation 3.8. Thus, the obtained result is an average, or a value, $a(t)$ close to Dirac delta function

$$w(t) * v(t) = a(t). \tag{3.10}$$

Convolving both sides of equation 3.1 with $v(t)$ gives an average of the reflectivity function

$$\begin{aligned} x(t) * v(t) &= r(t) * w(t) * v(t) \\ &= r(t) * a(t) \\ x(t) * v(t) &= \langle r(t) \rangle. \end{aligned} \tag{3.11}$$

It is common to discretize the output from the deconvolution and substitute in equation 3.7 to produce the discretized recursive formula

$$\tilde{\xi}_{j+1} = \tilde{\xi}_j \left(\frac{1 + \langle r \rangle_j}{1 - \langle r \rangle_j} \right), \quad j = 1, ..., N \tag{3.12}$$

where tildes denote quantities derived from averages of $\langle r(t) \rangle$ or their digitized form $\langle r_j \rangle$. Oldenburg et al. (1983) also showed that the logarithm of the normalized acoustic impedance estimated from the deconvolved seismogram is approximately an average of the true logarithm of the impedance.

Berteussen and Ursin (1983) have estimated two different nonlinear formulas to obtain acoustic impedance from seismic data (estimated reflection coefficients). Both formulas, one derived from discrete seismic model and the other from continuous seismic model, produce similar results for reflection coefficients.

The discrete nonlinear recursive formula to obtain the acoustic impedance is given by

$$\tilde{\xi}_{k+1} = \xi_1 \prod_{j=1}^{k} \left(\frac{1 + \langle r \rangle_j}{1 - \langle r \rangle_j} \right), \tag{3.13}$$

where ξ_1 is the acoustic impedance of the first layer and is assumed to be known.

In the continuous seismic model the elastic parameters vary continuously with depth or time (t). An estimate of the reflectivity function is written as

$$r(t) = \frac{1}{2} \frac{d[ln\xi(t)]}{dt}. \tag{3.14}$$

Inverting equation 3.14, an estimate of the acoustic impedance can be written as

$$\hat{\xi}(t) = \xi(0) e^{2 \int_0^t \hat{r}(u) du}. \tag{3.15}$$

A discretized version of the equation 3.15 can be represented as a recursive formula given by

$$\hat{\xi}_{k+1} = \hat{\xi}_k e^{2\hat{r}_k}. \;\; k = 1, 2, ..., \tag{3.16}$$

Berteussen and Ursin (1983) have shown that both formulas (equations 3.13 and 3.16) gives similar results. In fact, they differ less than 5% for $|\hat{r}_k| \leq 0.4$.

3.1.3 Estimation of acoustic impedance from band-limited seismic data

Seismic data acquired in field is always band-limited. Berteussen and Ursin (1983) have developed an approximation of the acoustic impedance model for band-limited data. In the continuous time data, the seismic model contains continuous time measurements. An estimate of the reflectivity function can be written as

$$\hat{r}(t) = \int_0^t r(t-u) p(u) du = r(t) * p(t), \tag{3.17}$$

where $p(t)$ is a band-limited seismic pulse. Using equation 3.15, an estimate of the acoustic impedance can be obtained

$$\hat{\xi}(t) \approx \xi(0)[1 + 2 \int_0^t \hat{r}(u) du]. \tag{3.18}$$

Taylor expansion can be applied into equation 3.18 only if the absolute value of the integrand is much less than 0.5. Additionally, it can be seen that the integrand in

equation 3.18 is the convolution of $\hat{r}(t)$ with the unit step function $n(t)$

$$n(t) = \begin{cases} 1 & t \geq 0, \\ 0 & t < 0. \end{cases}$$

Finally, equation 3.17 is used to compute the integrated seismic impulse

$$v(t) = p(t) * n(t) = \int_o^t p(u)du. \tag{3.19}$$

Berteussen and Ursin (1983) have shown that the estimated acoustic impedance minus the acoustic impedance in the top layer, is approximately equal to two times the acoustic impedance of the top layer times the reflectivity function convolved with the integrated seismic impulse. Usually, the estimated acoustic impedance from band-limited seismic data is obtained from the convolution between the true seismic impedance and the seismic pulse. However, Berteussen and Ursin (1983) derived that the estimate of the acoustic impedance minus the impedance in the top of the layer, is approximately equal to the true acoustic impedance convolved with the seismic pulse minus the acoustic impedance in the top of the layer times the integrated seismic pulse. That is

$$\hat{\xi}(t) - \xi(0) \approx [\xi(t) - \xi(0)n(t)] * p(t). \tag{3.20}$$

Generally, the seismic data is recorded in discrete form, Berteussen and Ursin (1983) developed an approximation for this case.

The estimate of the reflection coefficients is given by

$$\hat{r}_k = r_k * p_k = \sum_{j=-M}^{M} c_{k-j} p_j, \tag{3.21}$$

where p_k is a zero-phase band-limited seismic pulse.

It can be shown that the estimate of the discrete acoustic impedance can be written as

$$\hat{\xi}_{k+1} - \xi_1 \approx 2\xi_1 \sum_{j=1}^{k} \hat{r}_j = 2\xi_1 c_k * v_k, \tag{3.22}$$

where v_k represents the integrated seismic pulse

$$v_k = \sum_{j=-M}^{k} p_j. \tag{3.23}$$

As previously stated, the approximation in equation 3.22 is valid if the absolute value of the sum of the estimated coefficients $\hat{r}_j$ is much less than 0.5.

Equation 3.24 is the discrete approximation of the estimated acoustic impedance when the sum of the reflection coefficients r_j and the estimated coefficients $\hat{r}_j$ over all of the layers is much less than 0.5

$$\hat{\xi}_{k+1} - \xi_1 \approx \xi_{k+1} * p_k - \xi_1 v_k. \tag{3.24}$$

3.2 Sparse spike inversion

In order to extract a volume of acoustic impedance from the seismic data, Jason's software employs an inversion method performed over each trace of the seismic data. This trace based inversion implements a method called *Constrained Sparse Spike Inversion*, which has evolved from the original $l_1 - norm\ deconvolution$. The main advantage of the sparse spike inversion method is that it can be used as a full bandwidth estimate of the reflectivity with a few extra constraints, whereas the deconvolved reflectivity obtained from the common inverse filter is band-limited (Russell, 1988). In the following section, a brief explanation of the development of the algorithm is presented prior to the detailed implementation of the Jason's software.

Taylor et al. (1979) used the well known convolutional model to show that an approximation $\hat{r}$ of the spike train r from a given noisy trace can be estimated using the $l_1 - norm\ deconvolution$. The results obtained using $l_2 - norm\ deconvolution$ may be quite different than those obtained from $l_1\ norm$ or least absolute deviation criterion. A linear programing system can be used to solve this problems by minimizing the error ϵ between the observed data and the modeled data. Generally, the l_2 norm or least square is used as a criterion to minimize

$$\sum \epsilon_i^2. \tag{3.25}$$

However, l_1 can be used to minimize the error, and is called $l_1\ norm$ of ϵ

$$\sum |\epsilon_i|^1. \tag{3.26}$$

The $l_1\ norm$ is characterized by its robustness when compared with other methods. In other words, no major errors in the answer will be obtained when few bad data points are present in many reasonable data points.

Using the convolutional model, a noisy trace is expressed as

$$t(t) = r(t) * w(t) + n(t), \tag{3.27}$$

where r is the spike train and w and n are the wavelet and noise respectively. Assuming that the wavelet w is known, equation 3.27 can be written in matrix notation as

$$\mathbf{t=Wr+n}. \tag{3.28}$$

To find the spike train r using the , the equation 3.29 should be minimized

$$\lambda \sum r_j^2 + \sum n_i^2, \tag{3.29}$$

where the left-most term is analogous to prewhitening and λ corresponds to the amount of prewhitening. Using the l_1 *norm* definition, the prewhitening term will not destroy the isolated spikes and therefore will preserve them.

A weighted form of the equation 3.29 has shown to be more advantageous on ungained traces

$$\lambda \sum q_j |r_j| + \sum p_i |n_i|, \tag{3.30}$$

where the weights p_i include the effects of any tapper desired for a window, and the local average magnitude of the trace. Finally the problem expressed in 3.30 can be solved using any l_1 solution procedures. The same approach can be used to extract the wavelet if the spike train r is known.

Levy and Fullagar (1981) used l_1 $norm-deconvolution$ to reconstruct the sparse spike train from an incomplete set of Fourier components. In fact, they showed that 20% to 25% is sufficient to obtain high quality reconstruction.

This approach has a few advantages related to errors. In frequency domain, it is possible to identify the spectral data that are most contaminated. Additionally there is no attempt to minimize the misfit error, because minimization of this norm favors solutions with as few nonzero values as possible (Levy and Fullagar, 1981). This approach reproduces the original spike train with some minor differences that are related to non-uniqueness.

The spike recovery deconvolution considers the ground reflectivity as a succession of spikes separated by zeros. When this spiky reflectivity is convolved with a wavelet, it generates a seismogram with an accuracy that is consistent with the level of noise (Fullagar, 1985). Fullagar (1985) developed the theory of generalizing the l_1 $norm-deconvolution$ to l_p $norm-deconvolution$. His work enhances the importance of the knowledge of *a priori* information and takes into account all necessary information when deconvolving the seismogram. This method, has a non-unique solution, which may not represent the actual reflectivity.

The problem formulated by Fullagar (1985) is developed in frequency domain and considers that no information is known about the reflectivity outside the reliable data. Using only these data, the spiky reflectivity estimated both satisfies and fits

the data as closely as the true reflectivity. This can also be seen as an estimation of a model for which the degree of misfit is consistent with the level of noise. Then, it is clear, that the level of misfit between the observed seismogram and the noise free seismogram needs to be known. This estimation of misfit is given statistically by the normalized sum of squares residuals.

In the l_p *norm* $-$ *minimization* the coefficient matrix has an additive constant in the diagonal given by the Lagrange multipliers for the normalized square residuals. This multiplier stabilizes the matrix inversion. For l_p *norm* when $p = 2$, the problem is linear and the damped least squares solution can be computed. Contrarily, when $p \neq 2$ the problem becomes non-linear and the computation of the minimum l_p *norm* solution is achieved by improving iteratively the starting model. This formulation also allows the determination of the minimum l_0 and l_1 norm solutions.

The l_p *norm* $-$ *deconvolution* is an alternate method to improve the band-limited spectrum of the reflectivity train. This approach relates the generalized l_p *norm* and the distribution of the reflectivity and noise in the data. Debeye and van Riel (1990) showed that when the convolutional model exactly describes the seismic signal and the reflectivity is statistically independent of the noise, the maximum likelihood estimate of the reflectivity can be obtained by $l_p - norm$ *deconvolution*. Debeye and van Riel (1990) showed that the $l_p - norm$ *deconvolution* can be used in both frequency and time domain. In fact, they are equivalent when the noise is minimized with l_2 *norm*. It is important to recall that l_0 *norm* corresponds to a variable that is sparsely distributed, l_1 *norm* to an exponential distribution, l_2 *norm* to a Gaussian distribution and l_∞ *norm* to a uniform distribution.

Based on the previous formulation given by Taylor et al. (1979), Debeye and van Riel (1990) showed that the general $l_p - norm$ *deconvolution* can be expressed by

$$\lambda L_q(\mathbf{r}) + L_p(\mathbf{n}). \tag{3.31}$$

In order to obtain the best deconvolution result, *a priori* information of the distribution of the reflectivity and noise should be taken into account in $l_p - norm$ *deconvolution* by minimizing a weighted sum of the corresponding norms. A general assumption in seismic is that reflectivity is sparse and spiky, and the noise has a Gaussian distribution with zero mean. Therefore, an $l_p - norm$ deconvolution would correspond to minimize the $l_0 - norm$ of the reflectivity and the $l_2 - norm$ of the noise. However, the calculation of the $l_0 - norm$ is computationally difficult (Debeye

and van Riel, 1990). In order to overcome this problem, Debeye and van Riel (1990) showed that a sparsely distributed reflectivity and Gaussian noise are best estimated using the mixed l_1 *norm* for reflectivity and l_2 *norm* for noise. The resulting solutions for reflectivity are sparse and spiky.

In general, λ is unknown, and is considered as a trade-off parameter. Therefore, it can either emphasize the power of the estimated reflectivity relative to the power of the estimated noise or in contrary, it can emphasize the sparsity of the estimated reflectivity relative to the accuracy of the estimated reflectivity. An analytical expression for λ can only be obtained if both the reflectivity and noise are Gaussian and are minimized with an l_2 *norm* (Debeye and van Riel, 1990). However, it is still complex to be analytically optimized.

When minimizing the l_1 *norms* of the reflectivity and noise, the reflectivity will be underestimated if the signal to deconvolve is contaminated with noise. This underestimation can be increased if the level of noise is increased. The parameter λ has influence only on the resolution and not on the magnitude of the underestimation of the reflectivity or noise. In order to choose the best λ, the *a priori* power, the desired error and the desired resolution of the reflectivity and noise, and the objective function to be minimized are all parameters that need to be considered.

The inversion proposed in this work followed the minimization of the objective function given by Jason Geoscience Workbench (2002). The objective function is written as

$$OBJF = \sum_j |r_j|^p + \lambda^q \sum_j (d_j - s_j)^q + \alpha^{-1} \sum_j (t_j - z_j)^2, \tag{3.32}$$

where $\sum_j |r_j|^p$ is the reflectivity term, $\lambda^q \sum_j (d_j - s_j)^q$ is the seismic misfit term and the third term correspond to the penalty on the trend mismatch. The seismic misfit term is now weighted by λ, and d_j and s_j are the synthetic and seismic data respectively. The reflectivity term refers to a linear sum of the absolute values of the reflection coefficients ($p = 1$) and ensures a sparse solution, whereas the seismic misfit term is the sum of the squared residuals ($q = 2$). Essentially, it controls the fit between the seismic data and synthetics generated during the inversion. The trend mismatch helps to control low frequencies. It calculates the difference between the possible maximum and minimum values of acoustic impedance (constraints) and the acoustic impedance trend, where the trend and constraints are defined prior to the

inversion process. The weight α is a standard deviation by which the inversion is allowed to deviate from the trend.

Even though the reflectivity term is a sum of the absolute values, the result should be the smallest sum possible. This follows the fact that changes in acoustic impedance and therefore reflectivities in the earth, are quite small. It is also important to mention that the first two terms of the objective function cannot be minimized simultaneously, as small residuals only occur with a detailed model and a sparse model only occurs with a large data mismatch. Therefore, the two terms of the objective function need to be balanced by controlling λ.

3.3 Carbonate seismology and rock physics

3.3.1 Background

Carbonate rocks are of paramount importance for oil and gas exploration. In fact, they comprise more than 50% of the proven hydrocarbon reserves. Most of the studies of seismic acquisition and processing are based in siliciclastic environments, and fewer seismic studies have been done in carbonate reservoirs. The methods applied here are commonly applied in siliciclastic reservoirs, hence the importance of this study is to investigate the use of the acoustic impedance inversion as an efficient tool to characterize a carbonate reservoir.

Wilson (1997) describes carbonates as calcareous sediments composed of shredded and reworked remains of shelly invertebrate animals and calcareous algae, microscopic lime-secreting organism, and coated fecal pellets mixed with lime mud matrix. Unlike siliciclasts, which are transported, carbonates rocks are generally organically or geochemically grown in place. In order to precipitate or grow carbonate rocks some environmental conditions are needed to be met. They include water temperature (subtropical waters) and salinity, food supply, marine activity and platform slope and depth (photic zone) among others. Carbonates are composed mainly of aragonite, magnesium-calcite which are stable only in marine saline water. Once carbonate rocks are generated, they are subjected to diagenetic processes (physical or chemical) that alter or change dramatically their physical properties such as porosity and permeability. In fact they occur faster than that of siliciclastic rocks.

Deposition of carbonate sediments follow a consistent and predictable pattern

from which carbonate facies progression can be stablished. Facies ranges from deep offshore muds and turbidites, debris on the slope, reef tracts at the platform margin, deposition of lime mud in backreef shelf and shelf lagoons to tidal flats or evaporitic salts (Wilson, 1997). As previously mentioned, diagenesis plays an important role in carbonate rocks. Wilson (1997) points out three major diagenetic environments: shallow-marine depositional diagenesis, meteoric diagenesis in vadose and phreatic zones and postburial diagenesis. Major diagenetic processes include dissolution, replacement, dolomitization, cementation, fractures, recrystallization, neomorphism and compaction.

Description of physical properties of carbonate rocks are of top importance for petroleum exploration and production. One of the most difficult properties to characterize is the porosity of carbonate rocks since it has many origins. Generally, porosity of carbonates rocks is depositional, but it is also generated by diagenetic alteration or fracturing. Basically, diagenetic processes reduce or enhance porosity, whereas fractures create porosity. The most common porosity types found in carbonate rocks are: intercrystalline and interparticle porosity, moldic and intraparticle porosity, vug and channel porosity, fenestral porosity, fracture and breccia porosity.

Carbonate rocks have faster seismic velocities and are denser than siliciclastic rocks. When a carbonate strata are overlain by siliciclastic strata with comparable difference in velocities and densities it will produce large reflection coefficients resulting in sections with strong reflections. However, if the overlying strata are a carbonate strata with similar values of velocities and densities lower reflection coefficients are generated resulting in transparent reflections. The effects of diagenetic processes can be so strong that they degenerate the propagation of seismic waves through it, lowering the resolution of seismic data. This processes can radically alter the rock so that air or water-filled inhomogeneties can cause back-scatter and convert surface waves to compressional and shear waves. In more complex geological settings, where carbonate rocks are mixed with other lithologies some additional problems are encountered such as statics, imaging and resolution problems. When carbonate rocks are differentially weathered statics problems are generated. If the weathering is intense, rough topography can be created resulting in imaging problems. The resolution problem arises due to significant difference in seismic velocities between layers. The high seismic velocity of carbonate rocks produces long wavelength compared to those generated in siliciclastic rocks for a given frequency. This effect will reduce the ability to image

thin layers. Sometimes, even the most sophisticated seismic processing or imaging algorithms are not capable to improve the resolution or desired results (Palaz and Marfurt, 1997).

Porosity type not only controls hydrocarbon storage, migration and reservoir economics but also the seismic properties of carbonate rocks. Generally, carbonate rocks show different porosity types or combination of them such as vuggy, moldic, channel, fenestral, fracture, microporosity, interparticle and intraparticle porosity. Since different porosity types have different compressibilities the seismic waves are strongly affected. Velocity increases exponentially as the porosity decreases. Anselmetti and Eberli (1997) reported that at equal porosities, velocity differences can exceed 2500 m/s. Figure 3.3 shows the wide range of velocities and porosities for different pore types in carbonate rocks. Permeabilities also presents a wide dispersion with porosity. However, the trend shows that permeability exponentially increases with increasing porosity (Wang et al., 1991).

Other factors that affect seismic velocities in carbonates rocks are burial depth, age, density, pore fluid and mineral content. Burial depth does not produce significant changes in velocity. In fact, its sensitivity depends more on the compressibility of the pore due to the depth and therefore pressure. Samples taken from the Great Bahama Bank showed that some low velocities at great depths are caused by diagenetic processes other than compaction. Similarly, young sediments showed high velocites. Therefore, velocity predictions cannot be stablished in terms of depth or age (Anselmetti and Eberli, 1997). Theoretically, V_P and V_s should decrease as bulk density increases, but the compressible moduli increases faster than the bulk density, therefore velocities increase as bulk moduli increase (Wang, 1997). Theoretically, the fluid substitution does not affect the shear modulus of a rock. On the contrary, the compressional velocity is strongly affected. Experimental results in carbonate rocks do not always follow theoretical predictions by Gassmann and Biot's theory. In fact, the seismic velocites are much more complicated by pore types. For instance, if a rock has vuggy or moldic porosity, fluid substitution does not change the compressional velocity because pores are relatively incompressible. On the other hand, the fluid substitution will have larger effect in rocks with flat pores or grain contacts. It is clear that the seismic velocites are also influenced by fluid type. Gasses are extremely compressible, and brine and water change less dramatically than oil as temperature and pressure change (Anselmetti and Eberli, 1997). Experimental results performed

by Wang (1997) showed that seismic waves in dry or fully gas-saturated carbonate rocks are not dispersive. However, for partial and fully liquid-saturated carbonate rocks seismic waves are dispersive. This clearly shows that the dispersion is caused by pore fluids. Mineral content also affects the seismic velocity in carbonates. As previously mentioned carbonate rocks are mainly composed of dolomite and calcite, but other minerals can accompany them such as halite, anhydrite and gypsum. Halite and dolomite have the lower and highest compressional and shear velocity respectively.

Table 3.1 summarizes common physical properties and some statistics for dolomites and limestones (Mavko et al., 1998).

Table 3.1. Common physical properties for dolomites and limestones (Mavko et al., 1998).

Physical Property	Minimum	Maximum	Mean	Standard Deviation
DOLOMITE				
V_p (km/s)	3.41	7.02	5.39	0.69
V_s (km/s)	2.01	3.64	2.97	0.37
V_p/V_s	1.59	2.09	1.82	0.07
Porosity	0.00	0.32	0.13	0.06
Density (g/cm^3)	2.27	2.84	2.59	0.12
Impedance 10^7 $(kg/m^3m/s)$	0.78	1.93	1.40	0.23
LIMESTONE				
V_p (km/s)	3.39	5.79	4.63	0.66
V_s (km/s)	1.67	3.04	2.44	0.37
V_p/V_s	1.72	2.04	1.88	0.08
Porosity	0.03	0.41	0.15	0.09
Density (g/cm^3)	2.00	2.65	2.43	0.16
Impedance 10^7 $(kg/m^3m/s)$	0.69	1.51	1.43	0.22

Some theories were developed to estimate velocities, porosities, densities and compressibilities in porous rocks. However, they have limitations based on several

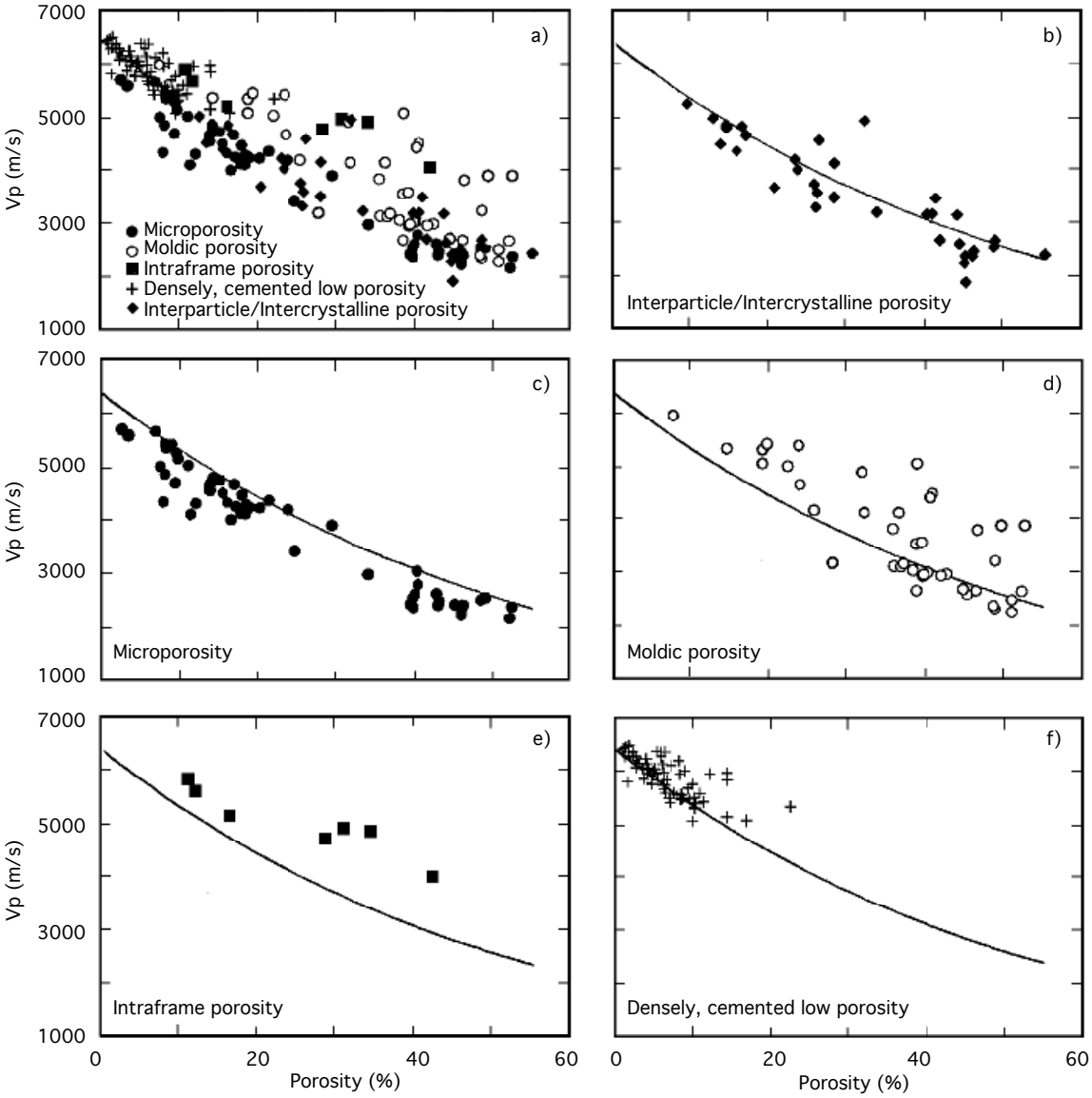

Fig. 3.3. Crossplot of porosity versus velocity for carbonates. (a) Predominant pore types. (b) Interparticle/Intercrystalline porosity. (c) Microporosity. (d) Moldic porosity. (e) Intraframe porosity. (f) Densely, cemented low porosity. Modified from Anselmetti and Eberli (1997) *in* Palaz and Marfurt (1997).

assumptions. Some of them work better for clastic rocks than for carbonate rocks. However, in this study, they will be extended to carbonate rocks to predict some physical properties and predict measured data.

3.3.2 Time-average equation

The time-average is widely used in sonic logs to compute porosity from sonic velocities. This equation previously developed by Wyllie relates the compressional velocity in a fluid-saturated rock to those in the solid rock matrix and pore fluid.

$$\frac{1}{V_p} = \frac{\phi}{V_f} + \frac{1-\phi}{V_m}, \tag{3.33}$$

where ϕ is porosity and V_m and V_f are velocities of the matrix and fluid, respectively. In general, equation 3.33 should not be applied to carbonate rocks with vugular porosity and fractures because this equation overestimates velocity due to the high compressibility of fractures and sensitivity of pore fluid saturation (Wang, 1997). Saleh and Castagna (2004) mention that rocks with interparticle and intercrystalline porosity are better described with Time-Average equation.

3.3.3 Gassmann equation

Gassmann's equation relates the bulk modulus of a fluid-saturated porous medium (K_{sat}) to the bulk moduli of the solid matrix, the frame and the pore fluid. The application of this equation is based on two main assumptions. First, the model assumes that the rock is homogeneous and isotropic, and the pore space is completely connected. Second, the equation is valid only at low frequencies, meaning that the wave frequency approaches zero. In this case the elastic modulus behaves quasi-statically

$$K_{sat} = K^* + \frac{(1-\frac{K^*}{K_0})}{\frac{\phi}{K_f} + \frac{(1-\phi)}{K_0} - \frac{K^*}{K_0^2}}, \tag{3.34}$$

$$V_p = \sqrt{\frac{3K_{sat}+4G}{3\rho_b}}, \tag{3.35}$$

$$\rho_b = \rho_g(1-\phi) + \rho_f\phi, \tag{3.36}$$

where K^*, G, K_f and K_0 are the bulk modulus of the porous rock frame, the shear

modulus of the rock frame, the bulk modulus of the pore fluid and the bulk modulus of the mineral matrix or solid rock, respectively. For low porosity rocks, most of the assumptions regarding the pore connectivity and pore type are violated. In carbonate rocks, these assumptions could be a problem due to the diverse pore type and low connectivity (Smith et al., 2003). Additionally, the presence of microcracks or cracks, uncertainties in the input parameters to the Gassmann equation and velocity dispersion can introduce errors when calculating velocities. Generally, the Gassmann equation predicts compressional and shear velocities that are lower than those measured in carbonate rocks.

In general, K^* in equation 3.34 is unknown and K_{sat} is known. Thus, it should be re-written in terms of known parameters. This equation is commonly used to compute frame (dry) or gas-saturated velocities (K^*) when V_p and V_s are available. The misfit between the Gassmann estimated and measured velocities has to be taken into account when computing frame velocities. This estimation works better in sandstones than in carbonates as well as at high effective pressures (Wang, 1997).

3.3.4 Biot's theory

The Gassmann approach is based on low frequencies. However, at higher frequencies (f$\rightarrow \infty$), this approach becomes inadequate, and the Biot's (1956) theory should be used. This theory covers the whole frequency range and predicts three different types of waves in a fluid-saturated porous medium: The fast compressional and shear waves (equations 3.37 and 3.38), and the slow compressional. The fast compressional and shear waves are analogous to the P and S waves in elastic solids, whereas the slow compressional wave is related to the motion in the pore fluid. At low frequencies the slow wave is diffusive, and the motion of this wave is described by the static Darcy's law. Contrarily, at high frequencies, the wave becomes propagational and the fluid flow is no longer governed by Darcy's law. However, this theory is not generally used since velocities increase from 1% to 3% as frequency increases from zero to infinity. Therefore, Gassmann equation is commonly used (Wang et al., 1991).

$$V_s = \frac{\mu}{\rho_d + (1 - \frac{1}{\alpha})\phi\rho_f}. \tag{3.37}$$

$$
\begin{aligned}
V_p &= \frac{A + [A^2 - 4B(PR - Q^2)^{1/2}]}{2B}, \\
A &= P\rho_{22} + R\rho 11 - 2Q\rho_{12}, \\
B &= \rho 11\rho 22 - \rho 12^2, \\
P &= \frac{(1-\phi)[1 - \phi - \frac{K_d}{K_m}]K_m + \phi\frac{K_d K_m}{K_f}}{D} + \frac{4}{3}\mu_d, \\
R &= \frac{\phi^2 K_m}{D}, \\
Q &= frac(1 - \phi - \frac{K_d}{K_m})\phi K_m D, \\
D &= 1 - \phi - \frac{K_d}{K_m} + \phi\frac{K_m}{K_f}, \\
\rho_{11} &= \rho_d - (1-\alpha)\phi\rho_f, \\
\rho_{22} &= \alpha\phi\rho_f, \\
\rho_{12} &= (1-\alpha)\phi\rho_f,
\end{aligned}
\tag{3.38}
$$

where α is the tortuosity factor and depends on the pore geometry of the rock.

Wang (1997) computed V_p and V_s Biot dispersions versus porosity, where the Biot dispersion is defined as the fractional difference between the velocities calculated from the Gassmann equation and by the Biot high frequency limit. For carbonates, the dispersion of V_p is less than 1%, whereas for V_s the dispersion is as much as $3\% \sim 4\%$. In Biot's theory, compressional velocities do not show much frequency dependence. Thus, it can be considered the same as compressional velocities estimated using the Gassmann approach. For shear velocities, the dispersion is related to the tortuosity factor. This factor has more impact in rocks with high porosities and high permeabilities.

It can be seen that carbonate rocks are challenging for oil exploration and production. Porosity variations on carbonate rocks have significant implications for production activities. As a result, it is important to integrate all geological, geophysical and engineering data available to construct a complete picture of the carbonate reservoir.

CHAPTER IV

METHODS

The digital data used in this study include a 3D seismic data (Amacker survey) of the Midland Basin, a suite of digital well-log data (gamma-ray, density, sonic and porosity logs) and checkshot data. Additionally, seismic horizons previously mapped by Merriam (1999) were used during the inversion. These data were combined to build the project and perform the inversion of acoustic impedance over the entire seismic survey.

In order to extract the full bandwidth acoustic impedance model, the flow shown in Figure 4.1 was followed. Once all data were loaded into the project, the first step was to tie the log data to seismic data in order to extract a wavelet for each well. These wavelets were used for the inversion of the band-limited acoustic impedance model. Alternatively, interpreted horizons were used in conjunction with acoustic impedance logs extracted from well data to build the geological model. This geological model allowed us to extract the low frequency content of it, which was then added to the previously generated band-limited acoustic impedance model. Finally, this full bandwidth acoustic impedance model was correlated with porosity logs to compute distribution of porosities of carbonate buildups.

4.1 Preparation of the data

The 3D seismic data used comprises an area of approximately 171,078,600 ft^2 (6.1 mi^2) (Figure 4.2). This data were previously processed to generate a post-stack section zero-phase volume was generated. Table 4.1 summarizes some of the acquisition parameters used to record the 3D seismic data.

Eleven vertical wells with their corresponding log data were used for the project (Figure 4.2). The log data used in each well contain gamma-ray, density, neutron porosity and sonic logs. Those wells that lack both sonic and density logs, or did not cover the entire depth of interest (i.e. the reservoir), were omitted from the study. One checkshot data was available in the area, and it was used for all wells to convert log data from depth domain to time domain. Gamma-ray logs were present in all wells,

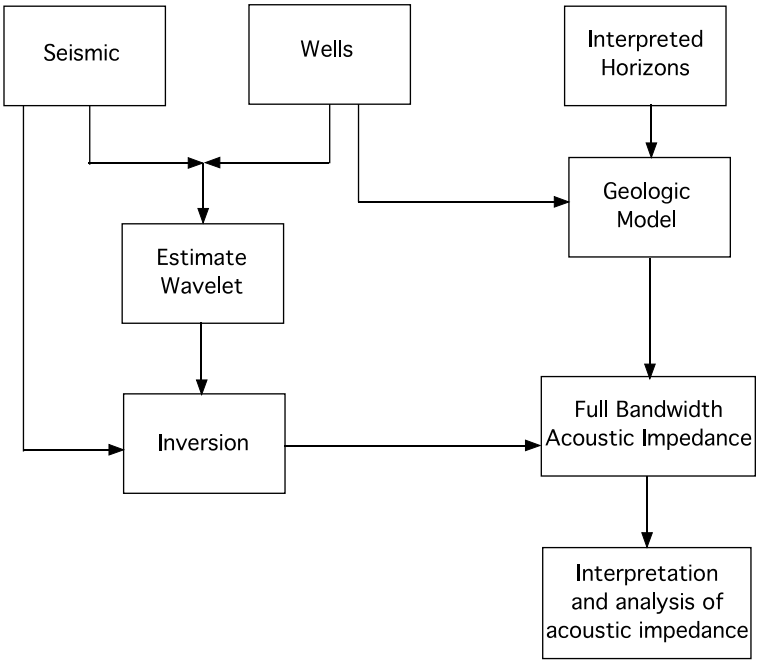

Fig. 4.1. Basic flow used for the inversion of the full bandwidth acoustic impedance volume (Jason Geoscience Workbench, 2002).

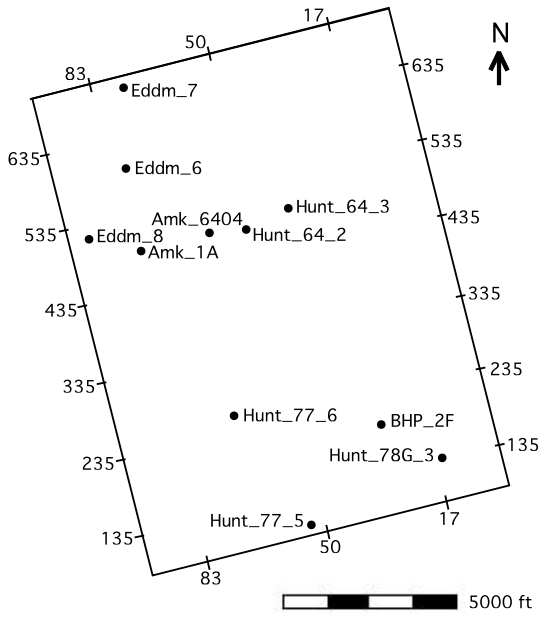

Fig. 4.2. Basemap of the Amacker survey and wells.

and they were used to identify and correlate important tops in the zone of interest with seismic data. Sonic logs were available in all wells, whereas density logs were not available for all of them. For those wells where density logs were missing, they were estimated using the Gardner equation in conjunction with sonic logs. Porosity logs were used to correlate and obtain a volume of distribution of porosities from the volume of acoustic impedance. Well data are of top importance during the tie process of log data and seismic data to ensure a reliable inversion of the acoustic impedance from seismic data.

Table 4.1. Acquisition parameters of the 3D Amacker survey.

Parameter	Value
Fold	24
Number of recording lines	18
Length of recording lines	2.5 mi
Number of vibrator line	48
Length of vibrator lines	2.85 mi
Cell size	110 by 115 ft
Acquisition type	In-line
Source line spacing	220 ft
Recording line spacing	660 ft
Group interval	230 ft
Vibrator point intervals	230 & 920 ft
Sweep length	12 sec
Listening time	4 sec

Two seismic interpretations previously mapped by Merriam (1999) were loaded into the project. These horizons were chosen since they not only describe the structure of the area, but also are important tops of formations present in the data set, namely, the top of the Tippet Shale and the top of the Strawn formation.

4.1.1 Well data completion

All log data was checked in detail and irregular peaks corresponding to erroneous measurements were cleaned out. This was done by comparing inconsistency of suspicious peaks through all well log data.

As previously mentioned, sonic logs were present in all wells. Unlike sonic logs, density logs were missing in some wells. In order to generate an estimate for missing density logs, the Gardner equation ($\rho = cV_p^n$) was used in conjunction with sonic logs.

Three wells with their original sets of density and sonic logs were used together to estimate the constants c and n of the Gardner equation by means of linear regression. Well Amk_64_2 was discarded due to the low correlation achieved, whereas wells Amk_6404 and Amk_1A showed a higher and more confident correlation values of regression coefficient (r). Figure 4.3 shows a plot of the logarithmic values of sonic data versus logarithmic density data for wells. The constant n measures the slope of the trend and constant c corresponds to the intercept of the trend with the vertical ($ln(\rho)$) axis. Both constants were computed in each plot and an average of the constant c was estimated as well as an average of the constant n. These averages produce an error of the estimated density log of 6.74% and 3.46% for wells Amk_6404 and Amk_1A, respectively. When compared with their corresponding estimated constants, errors of 6.28% and 3.39% were obtained. Errors obtained with averaged constants are also lower than those reached if constants were switched between wells (7.21% and 3.46% respectively).

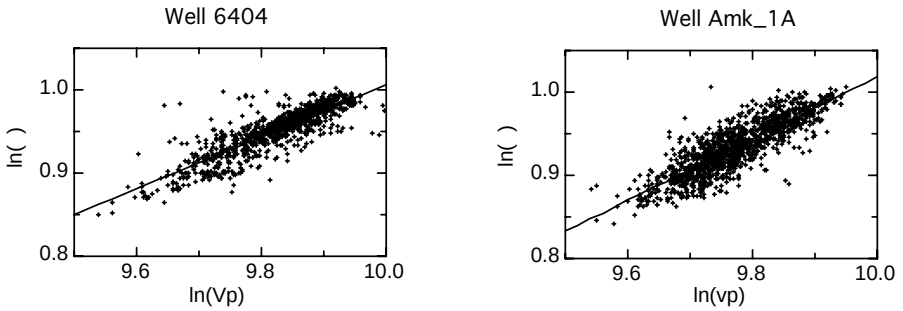

Fig. 4.3. Linear regression used in wells to estimate constants c and n in Gardner's equation. Average values of c (c_avg) and n (n_avg) are shown.

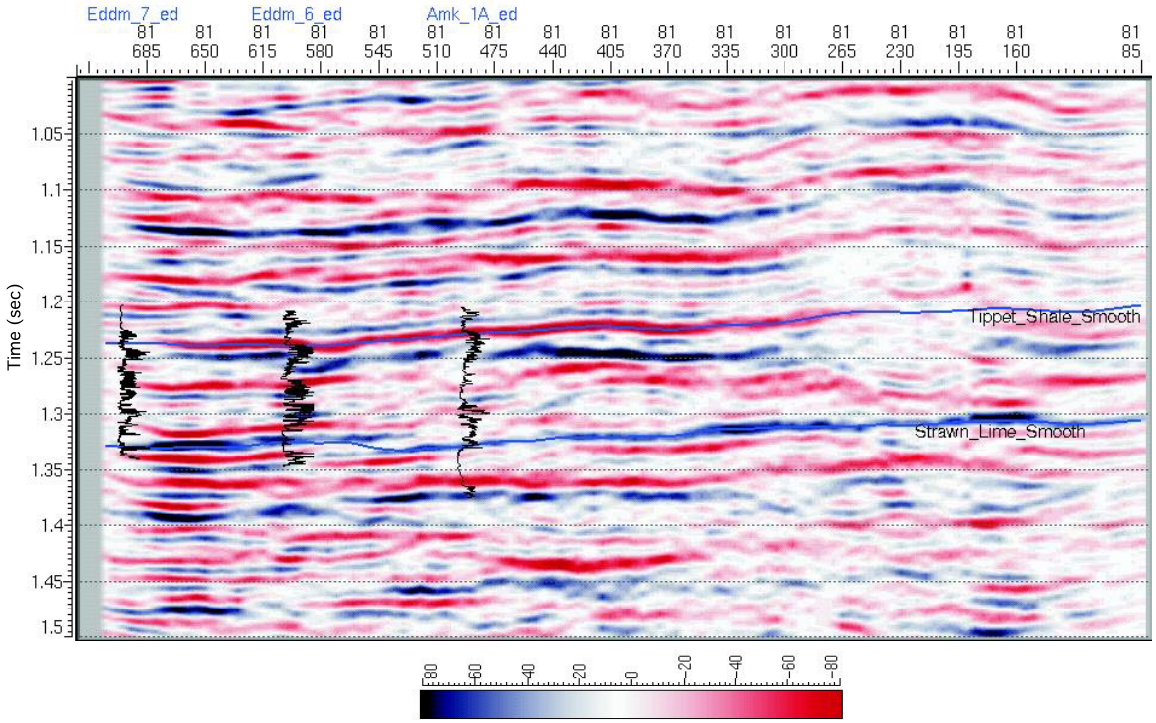

Fig. 4.4. Typical seismic line (In-line 81) and horizons used for inversion. Top of the Tippet shale and top of the Strawn formation.

4.1.2 Horizon interpretations

The Tippet Shale and the Strawn formation horizons loaded into the project are located above and below the reservoir, respectively and were picked in the zero-crossing. The horizons that correspond to the top and bottom of the reservoir itself were not loaded due to lack of resolution in the seismic data, and therefore low reliability (Figure 4.4). However, these tops are expected to be resolved during the inversion of acoustic impedance.

The original seismic interpretations were smoothed by applying a smoothing process available in Jason software. This was done in order to reduce peaks and sudden changes in the interpretation mapping. This process creates a smoothed version of the interpolated well-log acoustic impedance over the entire survey, given that the interpolation of geological model (acoustic impedance well data) runs along horizons. Figure 4.5 shows structural maps in time of the top of the Tippet shale and the top of the Strawn formation.

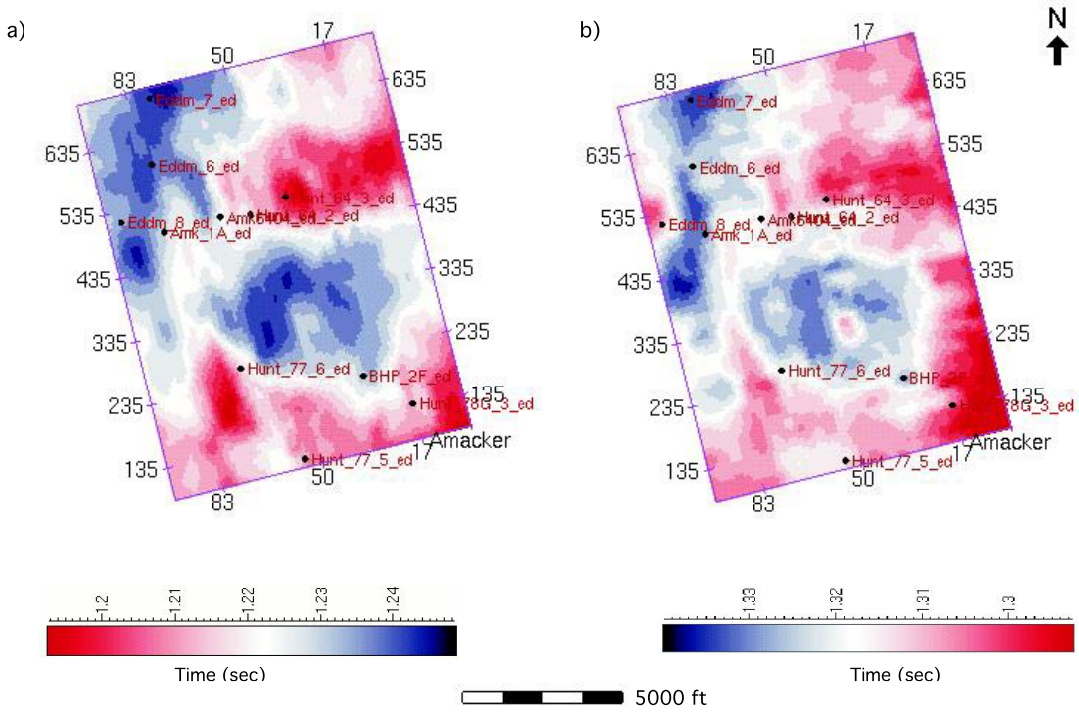

Fig. 4.5. Structural maps in time of the tops of the (a) Tippet Shale and (b) Strawn formation.

4.2 Synthetic seismograms

In order to tie the seismic data and well-log data, synthetic seismograms were created for each well. An iterative method was followed in which the estimated wavelet was improved during the tie process until an acceptable tie was reached.

The estimation of the wavelet followed a process similar to the algorithm described by White (1980). In this method, the wavelet amplitude spectrum is estimated using multiple seismic traces as input, and used to construct a zero-phase output wavelet. In order to ensure a good tie between seismic data and well data, a zero-phase wavelet was set for all wells, since the seismic data is also zero-phase.

The wavelet estimated is used to generate synthetic seismograms, and following the common stretch and squeeze process, the synthetics were matched with the seismic data. After each stretch and squeeze, the extraction of the wavelet was performed and the resulting wavelet was updated in the tie process again. This iterative method ensures a best tie of well log data and seismic data, as well as the extraction of the best wavelet (Jason Geoscience Workbench, 2002). This process was also supported

with top of the Tippet Shale and top of the Strawn formation identified on gamma-ray logs.

After the tie process, eleven wavelets were generated, corresponding to each well in the area. Since the inversion requires a wavelet (equations 3.27 and 3.28), those wavelets that show any inconsistency were eliminated for the future inversion. The wavelet generated in well Eddm_7 has higher frequency than the rest of the wavelets. This is probably due to the fact that the well is located on the border of the survey where seismic data has low signal to noise ratio and therefore lack of high resolution. For that reason, the presence of high frequency noise produces a high frequency wavelet. Consequently, the wavelet generated in well Hunt_77_5 was also eliminated from the inversion since it is located on the border of the survey where seismic data has lower quality as well. Even though the wavelet extracted here has no higher frequency content than Eddm_7, it will be shown that the inversion generated with this wavelet is as unacceptable as the one generated with the Eddm_7. Thus, the sensibility of the inversion was tested for different wavelets. Different types of wavelets were created, including averaged wavelets generated using all wells, only northern wells, only southern wells, or only one well. The computation of the averaged wavelets was based on the quality and location of wells in the survey.

4.3 Interpolation of well log acoustic impedance

Since the acoustic impedance inversion is band-limited, a low frequency model of acoustic impedance is required in order to generate the broadband acoustic impedance model. This low frequency model was extracted from interpolated well-log data and added to the band-limited acoustic impedance model extracted from seismic data.

At the depth of interest, an acoustic impedance log for each well was generated from density and sonic log. Four interpolation methods were tested in order to interpolate well log acoustic impedance data over the entire survey: Natural Neighbor, Locally Weighted, Triangulation, and Inverse Distance. Since the Natural Neighbor method is the most suitable when sparse data is available, it was chosen as the preferred interpolation method. In fact, this method provided the best interpolation results over the entire survey, since it produces a continuous and smooth interpolation of data. Figure 4.6 shows a comparison of the four interpolation methods along in-line 81. It can be observed that the Locally Weighted interpolation method (Figure 4.6b)

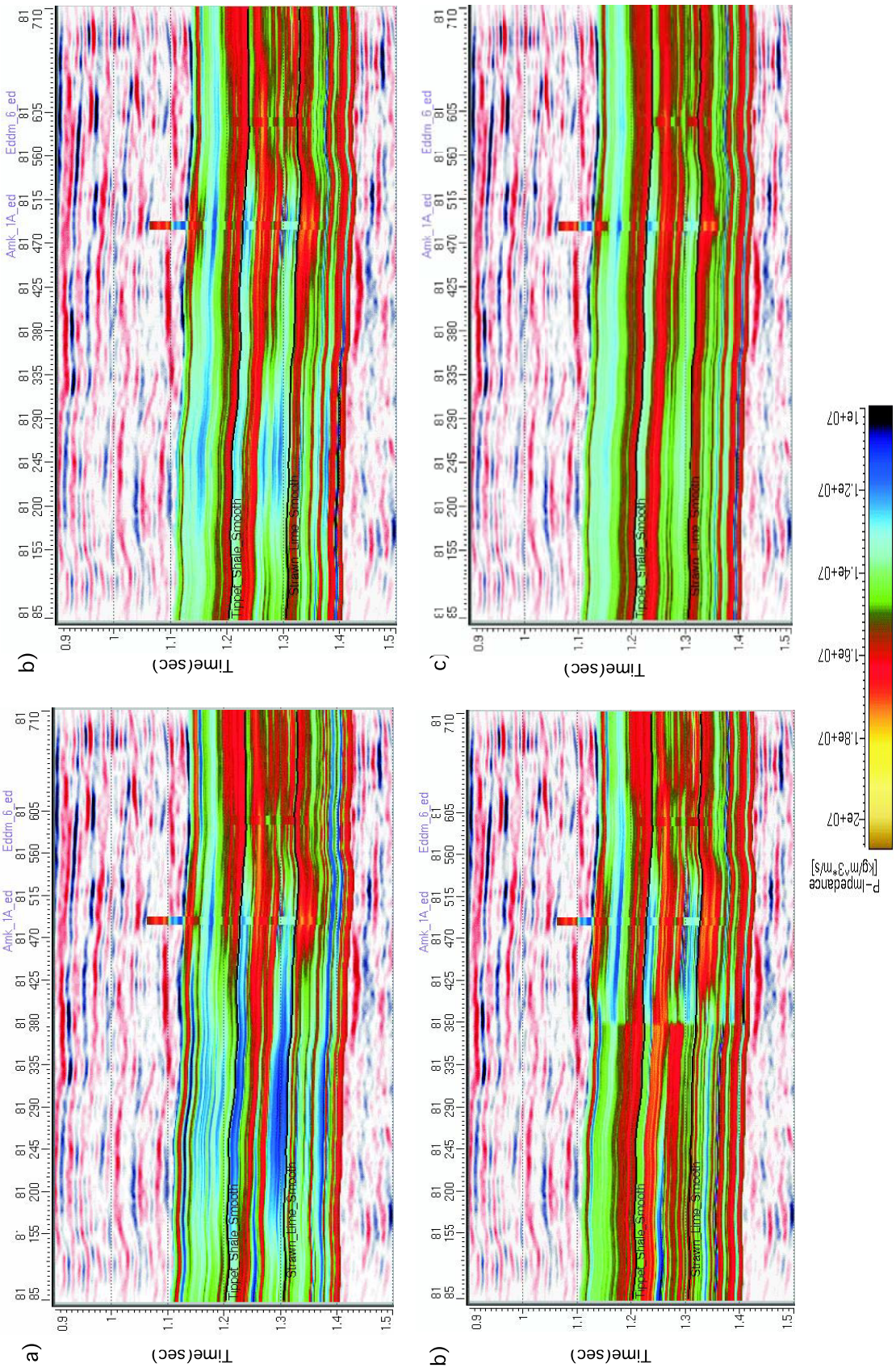

Fig. 4.6. Interpolation of acoustic impedance along in-line 81 for (a) Natural Neighbor, (b) Locally Weighted, (c) Triangulation and (d) Inverse Distance method.

gave similar results to the Natural Neighbor method (Figure 4.6a). However, interpolation is more concentrated close to the wells, less continuous over the survey and lacks of resolution or details. The Triangulation (Figure 4.6c) and Inverse Distance (Figure 4.6d) methods were not accurate for interpolating the data, since they introduced some effects that are not consistent with the geology of the area. They include sudden changes of interpolated data and rapid decrease of it away from the borehole respectively.

In order to quantify the difference between these interpolation methods and estimate their reliability, one trace of acoustic impedance generated with each method was extracted for four different locations along in-line 81 (Figure 4.7a). It can be observed that the quality of the interpolation gradually decreases with distance from wells (trace 145). Figure 4.7b shows the error of each interpolation method for the same traces compared to Natural Neighbor method along in-line 81. It is clear that the error also increases gradually away from the well. The largest error is given by the Inverse Distance method.

Figure 4.8 shows time slices of acoustic impedance extracted from the depth of interest (increasing in time from Figure 4.8a to 4.8f) for the Natural Neighbor method. Figure 4.8a and 4.8f show a widely spread distribution of low values of acoustic impedance response (1.1 kg/m$^3\times$ m/s to 1.4 kg/m$^3\times$ m/s) over the study area. These values correlate with the regional Tippet Shale over the reservoir, and the regional Canyon-Cisco-Wolfcamp shales below it. Figures 4.8b, 4.8c, 4.8d, and 4.8e correspond to the characteristic acoustic impedance response of the carbonate buildup interval (1.3 kg/m$^3\times$ m/s to 1.7 kg/m$^3\times$ m/s).

In order to generate the broadband acoustic impedance model, a filter was applied to the model generated from log data. This will extract the low frequencies only and, add to the band-limited model extracted from input seismic data. This process is explained in the next chapter as part of the final step of the inversion.

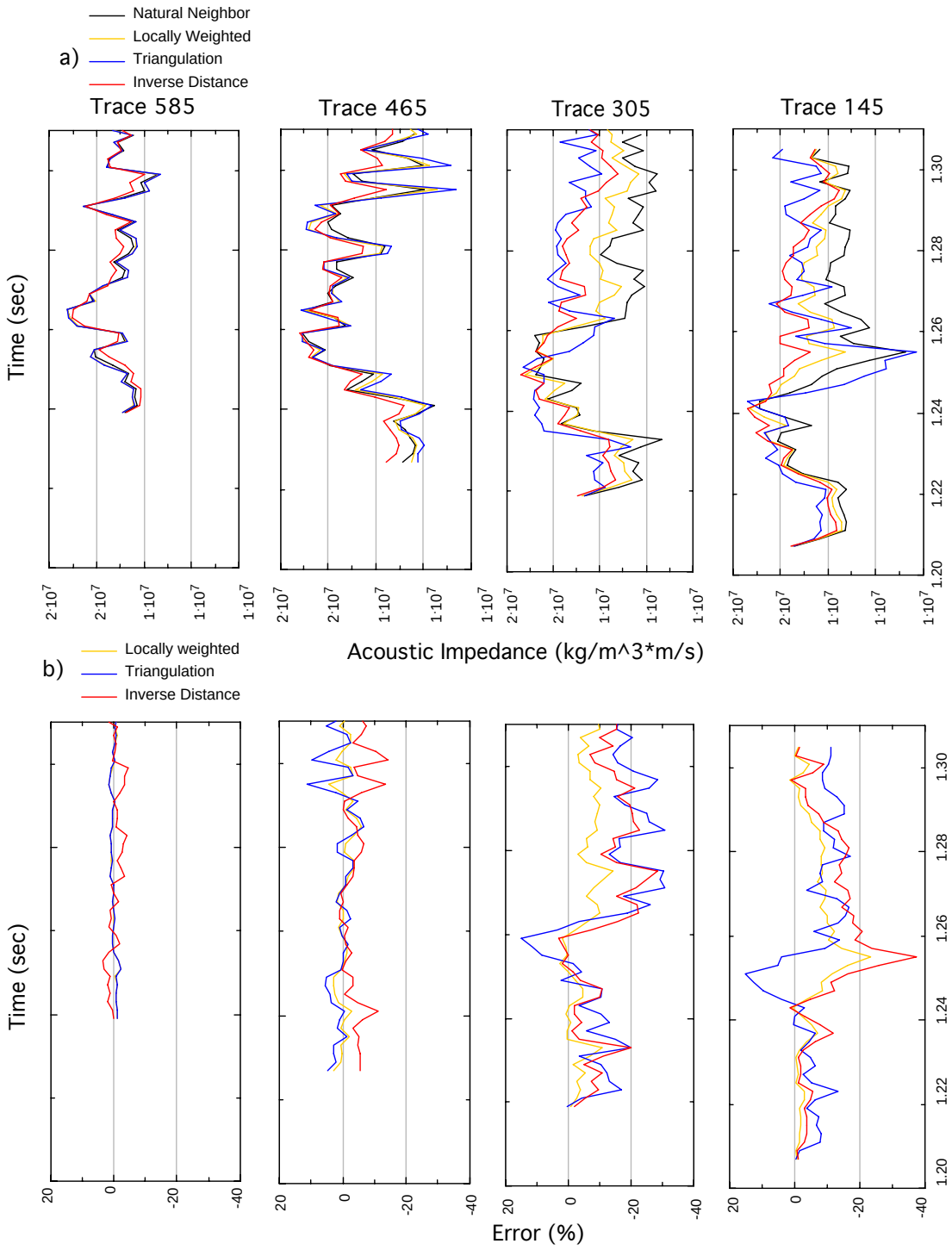

Fig. 4.7. (a) Traces of interpolated acoustic impedance generated from four different interpolation methods, Natural Neighbor (Black), Locally Weighted (Yellow), Triangulation (Blue) and Inverse Distance (Red) along in-line 81 . (b) Interpolation error compared to Natural Neighbor along in-line 81 for same traces.

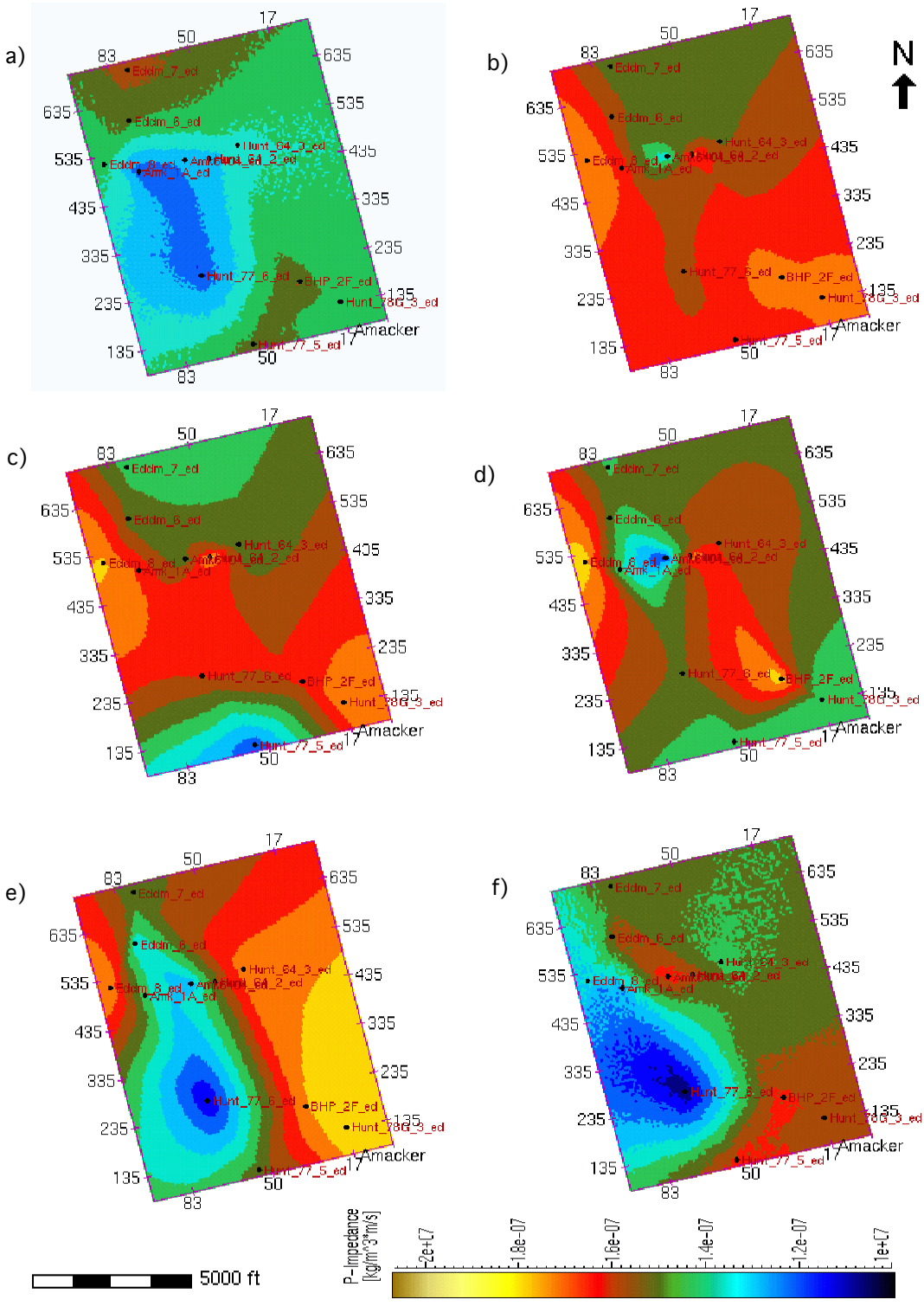

Fig. 4.8. Time slices of interpolation of the acoustic impedance using the Natural Neighbor method. (a) Maps the regional Tippet shale. (b), (c), (d) and (e) correspond to the carbonate reservoir zone and (f) maps the regional Canyon-Cisco-Wolfcamp shales.

CHAPTER V

RESULTS AND DISCUSSION

5.1 Results

Once the wavelets and the interpolation of acoustic impedance logs were computed, the inversion process is achieved by setting additional parameters or constraints. They include the selection of lambda (λ), trend mismatch, maximum and minimum values of acoustic impedance that the inversion can achieve and the p and q parameters for reflectivity and seismic misfit term as shown in equation 3.32. In order to choose those constraints a series of QC-tests were performed. These tests will also give an insight of the result of the final inversion.

5.1.1 Sparse spike inversion

The first parameter to control during the QC-tests is the maximum and minimum allowable value of the acoustic impedance and the trend mismatch. These parameters help to constraint the non-uniqueness of the inversion and are controlled interactively by using well log acoustic impedance as a reference. The trend mismatch essentially sets the trend of the acoustic impedance based on the trend of the acoustic impedance well log data. It was set to 1.45e07 kg/m$^3\times$ m/s at the top of Tippet Shale to 1.42e07 kg/m$^3\times$ m/s at the bottom of Strawn Formation. The maximum and minimum allowable values of the acoustic impedance is also set manually and is controlled by using acoustic impedance logs as a reference. All wells were displayed at the same time in order to select limits that properly covers the acoustic impedance well log data. Setting limits too tight to the well log acoustic impedance will considerably reduce the signal to noise ratio of the inverted acoustic impedance and some high or low values of acoustic impedance will not be properly inverted. Alternatively, if the limits are far from well log acoustic impedance log, erroneous high and low peaks of acoustic impedance would be inverted resulting in wrong interpretations. Therefore, limits near to the edges of the well log were used. For lower constraints 5.15e6 kg/m$^3\times$ m/s and 5.35e6 kg/m$^3\times$ m/s at the top of Tippet Shale and Strawn

Formation respectively and for upper constraints 2.27e7 kg/m$^3\times$ m/s and 2.31e7 kg/m$^3\times$ m/s at the top of Tippet Shale and Strawn Formation. This ensures that the inversion will generate acoustic impedance values from seismic data within these limits. During QC-tests and inversions, these parameters were less sensitive than the selection of the wavelet and λ. These constraints enter in the third term of the equation 3.32 where it calculates the difference between the limits and the trend of the acoustic impedance.

The next parameter to select is lambda (λ), which enters in the second term of the equation 3.32. In order to determine its optimal value, a well, or several wells can be selected. The software takes few traces adjacent to those wells (user selection) and runs a series of trial inversions over a range of lambda. It then compares the results of those inversions with the acoustic impedance log from selected wells. When the QC is performed, four plots are displayed that help to estimate the optimal value of lambda (Figure 5.1). The first plot requiring analysis is the signal to noise ratio reached by the inversion. This parameter measures the ratio of the normalized amplitude of the input seismic to the noise or residuals obtained during the inversion. The signal to noise ratio will give an insight of the signal to noise ratio of the final inversion since it will achieve similar values. Another important parameter to consider is the crosscorrelation, which compares between the trial inversions and the well log acoustic impedance. This parameter, along with the signal to noise ratio should be as high as possible to ensure best results during the final acoustic impedance inversion. The third plot to be studied is the seismic misfit. This represents the misfit between the inverted traces and the traces selected on the wells. Finally the last plot to be checked is the reflectivity. This parameter corresponds to the sum of the inverted reflectivity. As previously shown in equation 3.32 the seismic misfit term should decrease as much as possible, whereas the reflectivity term increases until the smallest sum is reached (Figure 5.1).

During the selection of λ, three traces were chosen as QC traces for each well. Different wavelets were also tested during the process. They included individual wavelets and averaged wavelets. Best results were obtained using a wavelet computed as an average from all eleven individual wavelets generated during the seismic and log tie process. This is probably attributed to the fact that this wavelet best represents the seismic characteristic of the entire survey. The QC results were similar for all individual wells. As expected, lower quality results were obtained when individual

wavelets corresponding to wells Eddm_7 and Hunt_77_5 were chosen. This result is reasonable since these wells are located close to the borders of the seismic survey where seismic traces have low signal to noise ratio, and consequently, the wavelet generated for those wells during the tie process has higher frequency than the rest of the wavelets. As a result, a wavelet extracted as an average of the eleven wells seemed to be the optimal wavelet to be used during the inversion.

During QC-tests, the signal to noise ratio was close to 30 db ± 3 db for all wells, but decreased if wavelets corresponding to wells Eddm_7 and Hunt_77_5 were used. For this case the signal to noise ratio dropped to 24 db and 16 db respectively. The seismic misfit for all wells was close to 1± 50%. For wells Eddm_7 and Hunt_77_5 the seismic misfit was considerably higher, about 2±1 and 3 ±1 respectively. The crosscorrelation was more variable for all wells achieving values around 0.45 ± 20%. For wells Eddm_7 and Hunt_77_5 those values were lower, 0.35 ± 20%. Reflectivity misfit was also similar for all wells, 0.009 ± 40%, whereas, for wells Eddm_7 and Hunt_77_5 this value was higher 0.03 ± 0.01. These tests were run over a range of λ that varied from 1 to 50. Figure 5.1 shows an output of these tests. It can be observed that for large values of λ, the seismic misfit remains stable or does not significantly decrease. Additionally, neither the signal to noise ratio nor the well log correlation increases further. Moreover, choosing higher values of λ could decrease the value of the correlation. Then λ=26 was chosen as the optimal value to be used during the inversion process.

From previous results, we expect that the inversions generated with wavelets extracted from wells Eddm_7 and Hunt_77_5 have lower quality and therefore they will not be considered. Several inversions were generated to determine which wavelet extracted from wells produces the best inversion with the highest signal to noise ratio, correlation value and lowest seismic misfit. In order to run these tests, several wavelets were used. They included a wavelet computed as an average from all wells, average from the northern wells, average from the southern wells, from all wells except wells Eddm_7 and Hunt_77_5 and from individual wells. The trend mismatch and the parameter lambda ($\lambda = 26$) were kept constant. In order to quantify these results, histograms and statistical analysis (not shown here) of maps of signal to noise ratio and correlation were performed. Inversions generated with individual wavelets achieved a mean value of signal to noise ratio of 28 db and well log correlation of approximately 0.97. Averaged wavelets produced the highest mean signal to noise

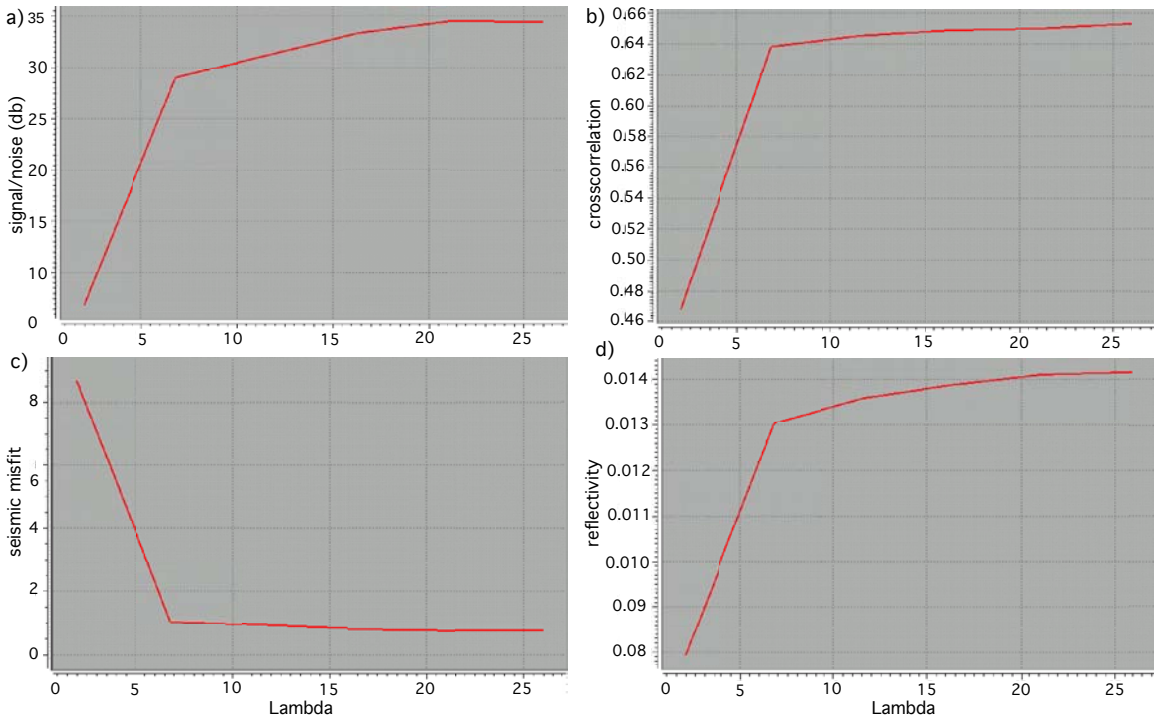

Fig. 5.1. (a) Signal to noise ratio, (b) crosscorrelation, (c) seismic misfit, (d) reflectivity.

ratio of 30 db and well log correlation of 0.99. As expected, maps of the signal to noise ratio and correlation showed that the inversions generated with wavelets corresponding to wells Eddm_7 and Hunt_77_5 had lower values. They achieved 16 db and 0.95 respectively. Therefore, these results were discarded. Additionally, based on a comparison of statistical analysis, the most confident inversion is achieved when an average of all wavelets is used.

Since the signal to noise ratio considers residuals as noise, a perfect inversion with virtually no residuals would have a very high signal to noise ratio, meaning that all data was perfectly inverted, including noise. Therefore, the interpretation of the signal to noise ratio could be misunderstood. In order to confirm the validity of the inversion, a plot of the inverted synthetics and seismic data was generated, as well as the inverted residuals as the inversion progressed. Figure 5.2a shows the inverted synthetics and the seismic data for three QC-traces. It can be observed that the match is improved for higher values of lambda. Similarly, residuals decrease as the inversion progresses (Figure 5.2b).

Figure 5.3a shows the final inversion for the inverted synthetics over the input

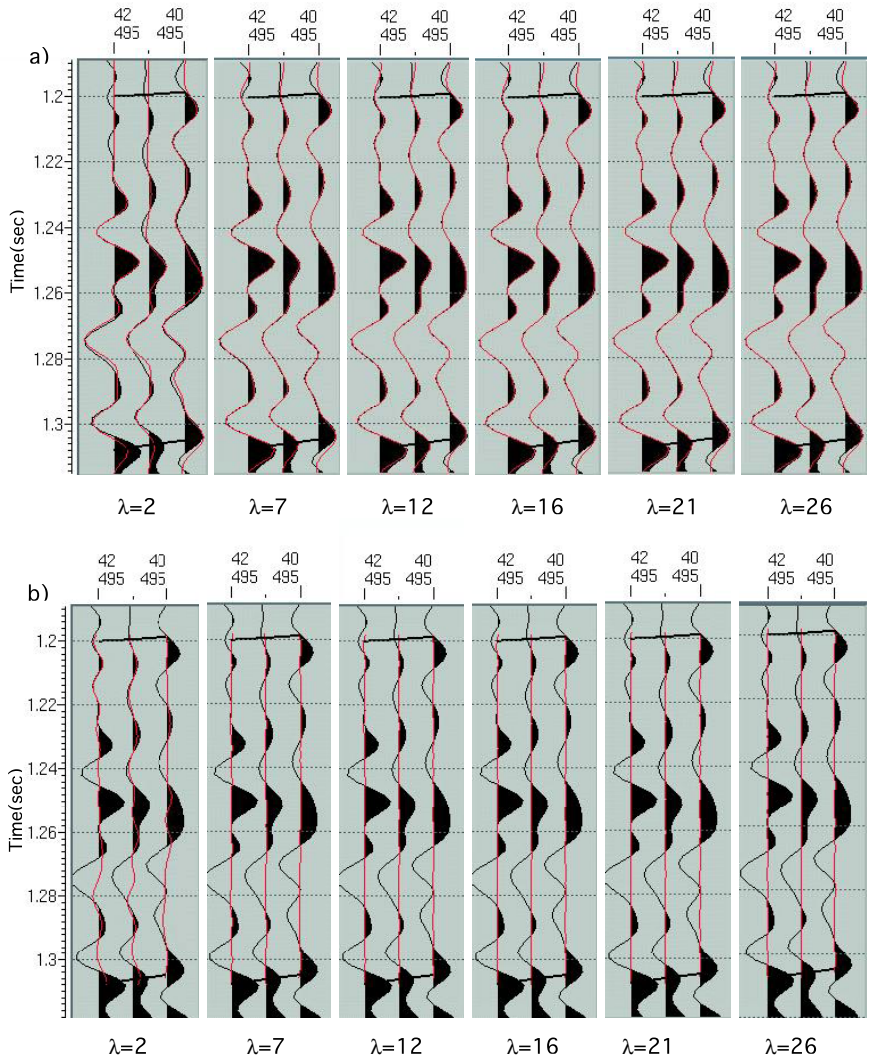

Fig. 5.2. (a) Inverted synthetics and (b) residuals (red) for different values of lambda (λ).

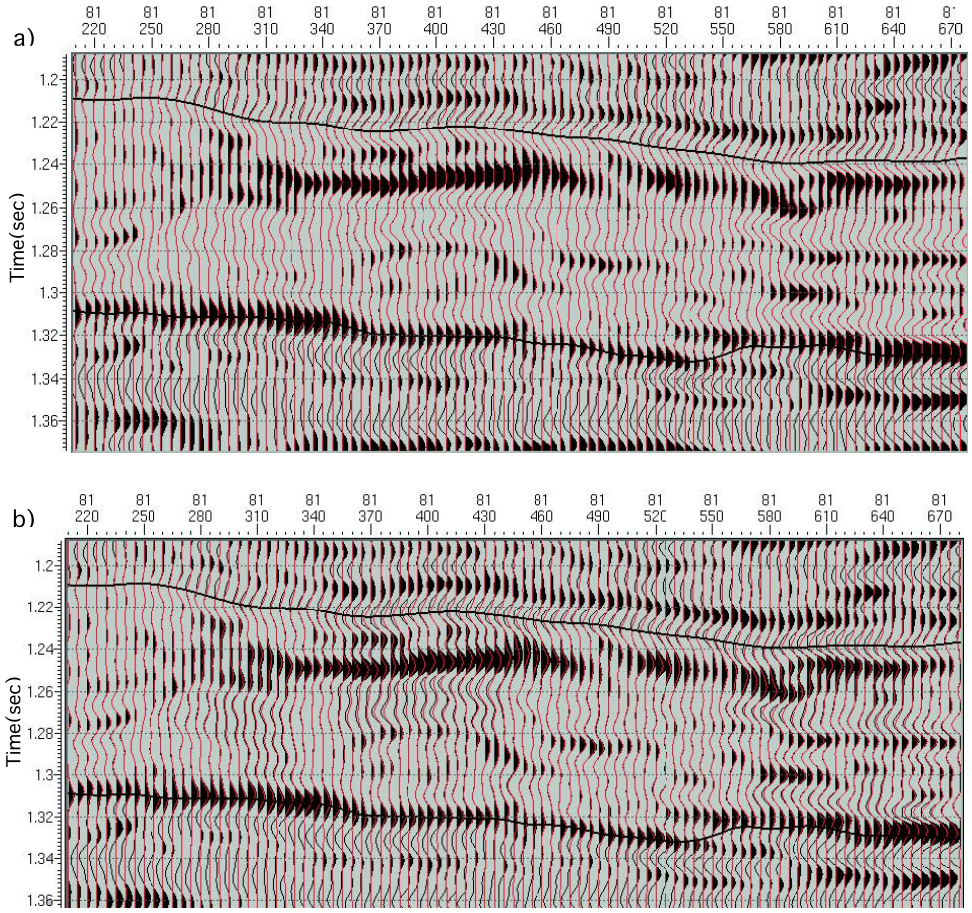

Fig. 5.3. (a) Inverted synthetic data (red) from averaged wavelets, (b) synthetic data (red) using wavelet from well Hunt_77_5.

seismic data along inline 81. It can be clearly seen that synthetics match the seismic data over the depth of interest. Figure 5.3b shows that the synthetics do not match the seismic data if an incorrect wavelet is used (Eddm_7 or Hunt_77_5). Figure 5.4a and Figure 5.4b show the residuals over the input seismic data in time and frequency domain respectively. In the frequency domain, the residuals (noise) have higher amplitudes beyond the frequency content of the inverted/seismic data. If the wrong wavelet is used during the inversion, the residuals would shift within the seismic bandwidth.

These results clearly show the importance of the selection of a wavelet and the sensitivity of the inversion to this parameter. Figure 5.5 shows two acoustic impedance sections generated using different wavelets. It is clear that the section generated with the averaged wavelet (Figure 5.5a) shows more details of the vari-

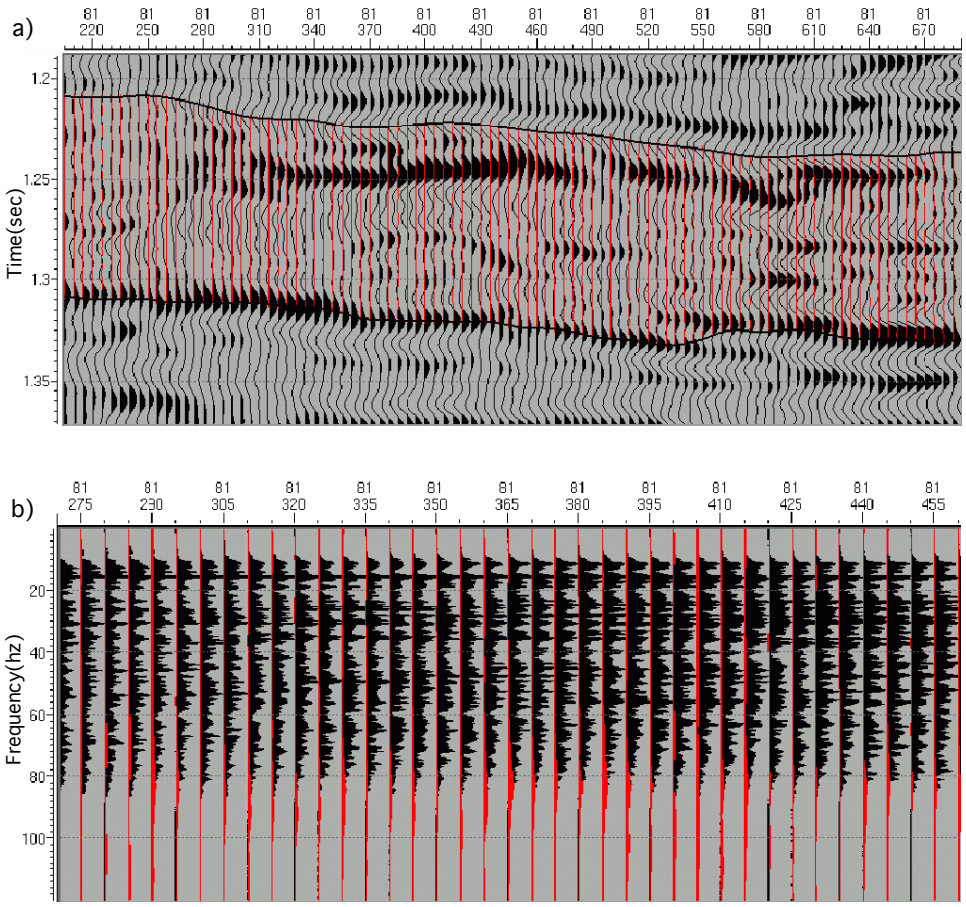

Fig. 5.4. (a) Inverted residuals (red) from averaged wavelets, (b) frequency spectrum of the input seismic data and inverted residuals (red).

ations of the acoustic impedance, whereas, the section generated with the wavelet corresponding to well Hunt_77_5 (Figure 5.5b) lacks of details and some acoustic impedance are not properly inverted (black spots).

Thus so far, a volume of acoustic impedance response has been generated. This volume is band-limited since low frequency content of the interpolated well logs acoustic impedance has not been added yet. At this stage, two new horizons were mapped to define the productive zone. The scope of this mapping is to extract the acoustic impedance data from this interval and compute statistical attributes such as maximum, minimum, average, mean, median and standard deviation at each trace. Maps of these statistical attributes were generated to correlate them with the known locations of carbonate buildups and determine the presence of new ones as well. Figure 5.6

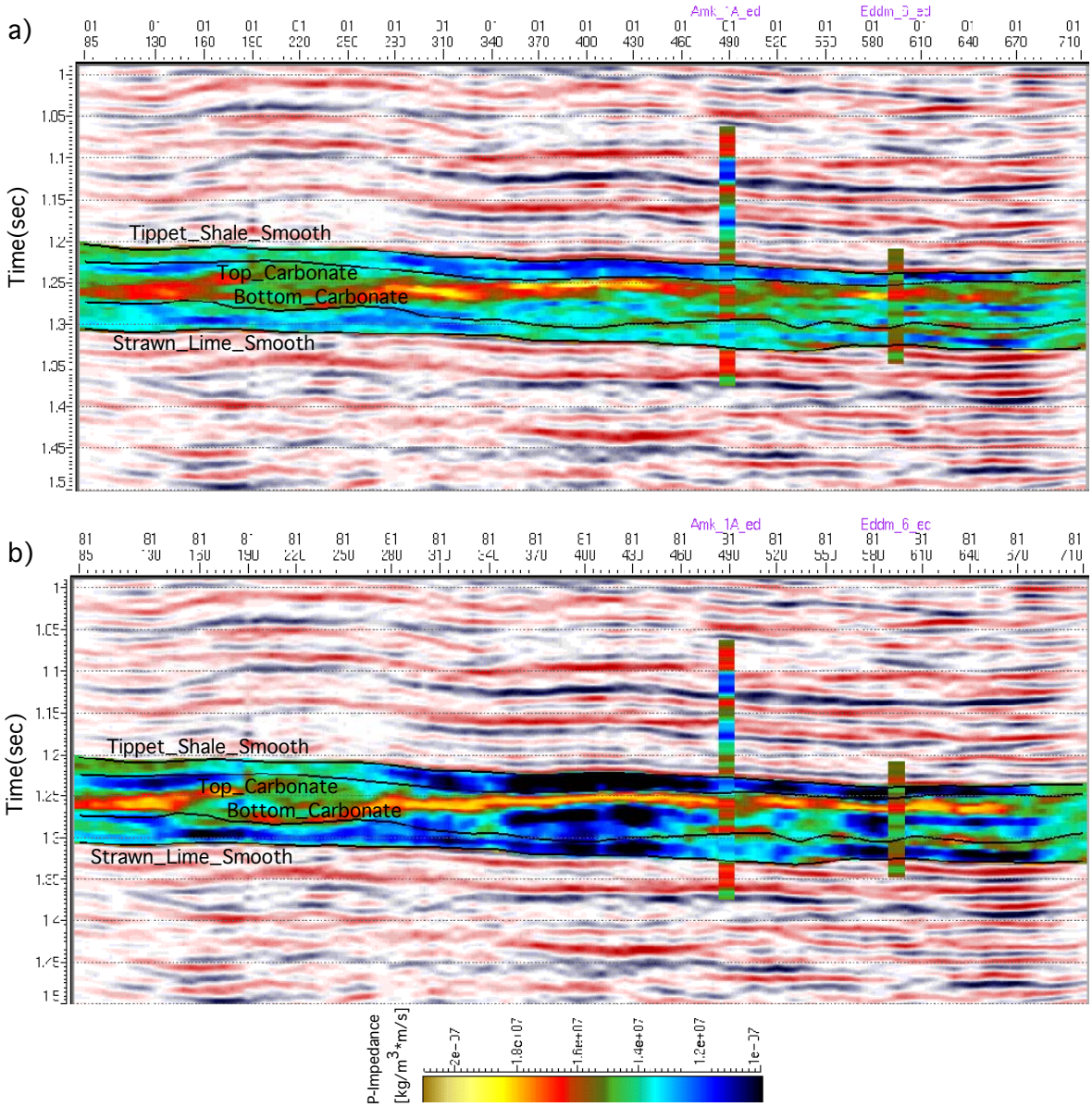

Fig. 5.5. (a) Inverted acoustic impedance using an averaged wavelet. (b) Inverted acoustic impedance using a wavelet from well Hunt_77_5.

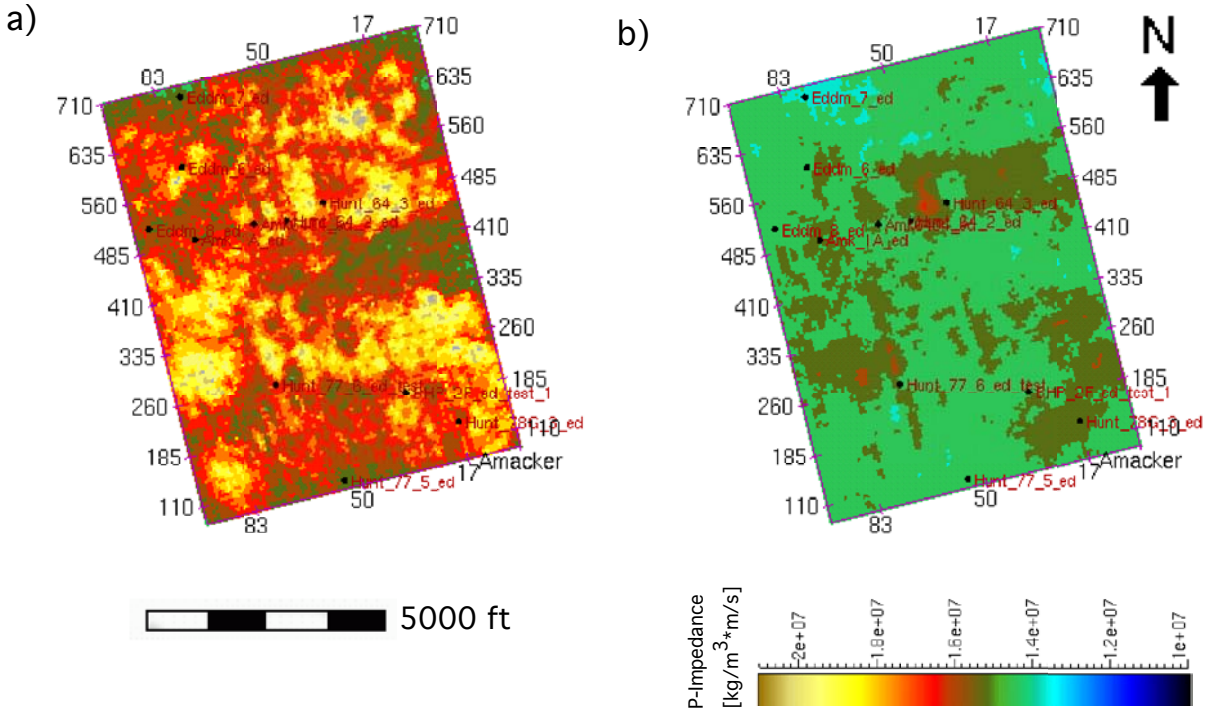

Fig. 5.6. Band-limited acoustic impedance attributes across the productive zone. (a) Maximum statistical attribute and (b) average attribute.

shows a map of the maximum and average (rms) statistical attributes. The maximum statistical attribute shows a detailed image of the distribution of the maximum values of acoustic impedance. These values ranged from 1.41e7 kg/m$^3\times$ m/s to 2.14e7 kg/m$^3\times$ m/s. On the contrary, the average (rms) attribute shows a more uniform value over the entire survey (1.36e7 kg/m$^3\times$ m/s to 1.63e7 kg/m$^3\times$ m/s). This is probably due to the fact that the inverted acoustic impedance model lacks of sufficient resolution since the low frequency component is still missing.

5.1.2 Broadband acoustic impedance inversion

The frequency bandwidth of the input seismic data ranges from approximately 10 $\sim$ 80 Hz. (Figure 5.4b). Consequently, the acoustic impedance model extracted from it would be band-limited as well (10 $\sim$ 80 Hz.). In order to generate a broadband (0 $\sim$ 80 Hz.) acoustic impedance model of the carbonate reservoir, the low frequency content of the well log acoustic impedance model (0 $\sim$ 10 Hz.) was added to the band-limited acoustic impedance model extracted from seismic data. A bandpass

filter and a highcut filter were applied to the band-limited and well log acoustic impedance model, respectively, and added together to generate the full bandwidth acoustic impedance volume. For the bandpass filter (trapezoidal shape) the limits selected were 0, 20, 50, 70 Hz. The highcut filter applied to the interpolated well log acoustic impedance model had 0, 20 Hz limits, with an overlap in 10 Hz. The final bandwidth of the model was 0, 50, 70 Hz. with a high overlap of 20 Hz. Higher frequencies (up to 80 Hz.) were not included in the filter. At these high frequencies, residuals have considerably strong amplitudes (Figure 5.4b). If they are included, a coarser and noisier output is generated, whereas, frequencies up to 70 Hz. produce a smoother and less noisy model of acoustic impedance which correlates better with the seismic data.

As predicted, the new volume of acoustic impedance generated has higher resolution than the band-limited model. This is achieved since not only the high frequency content is necessary for increasing the temporal resolution, but also the low frequency component is important. Figure 5.7a shows the band-limited input seismic section. Figure 5.7b shows the inversion for the band-limited acoustic impedance model for the same section. The poor resolution of changes in acoustic impedance is noteworthy, Figure 5.7c shows the section of full bandwidth inverted acoustic impedance model. It can be observed that there is a clearer image of changes in acoustic impedance. Additionally, the match between wells and the inverted acoustic impedance is considerably improved at their locations.

As part of the study, a volume of acoustic impedance corresponding to the productive zone was extracted once more to compute same statistical attributes as before. Now, it is clear from Figure 5.8 that there is a clear and more detailed response of the attributes over the entire survey for the full bandwidth model. Only the maximum (Figure 5.8a) and average (rms) acoustic impedance attributes (Figure 5.8b) are displayed since they give superior image of the distribution of the acoustic impedance. In addition, an isopach map of the Amacker formation was generated to correlate statistical attributes with its thickness. It can be seen that maximum acoustic impedance attribute varies from 1.40e7 kg/m$^3\times$ m/s to 2.07e7 Kg/m$^3\times$ m/s and average (rms) acoustic impedance varies from 1.33e7 kg/m$^3\times$ m/s to 1.69e7 kg/m$^3\times$ m/s. Mavko et al. (1998) reported theoretical minimum, maximum and mean values of acoustic impedance for common dolomites as 0.78 kg/m$^3\times$ m/s, 1.93 kg/m$^3\times$ m/s and 1.40e7 kg/m$^3\times$ m/s respectively and for limestones as 0.69 kg/m$^3\times$ m/s, 1.51kg/m$^3\times$ m/s

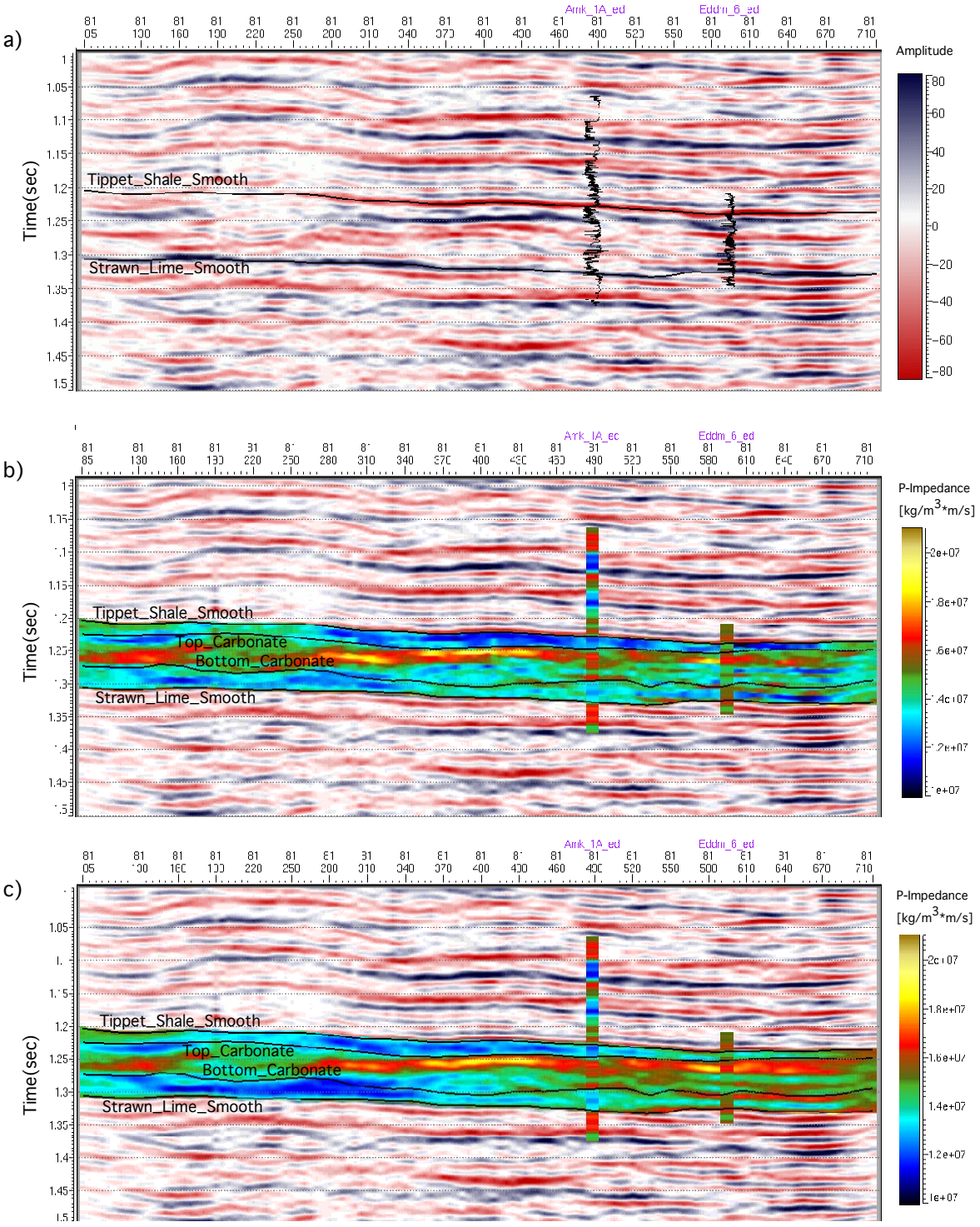

Fig. 5.7. (a) Input seismic data, (b) band-limited acoustic impedance inversion, (c) broadband acoustic impedance inversion. Acoustic impedance well logs are also displayed.

and 1.43e7 kg/m$^3\times$ m/s respectively. Results previously obtained are considered acceptable since they correlate with theoretical values. This leads to consider an arbitrary low values of average (rms) acoustic impedance lower than 1.45 kg/m$^3\times$ m/s (light green areas in Figure 5.8b), and lower than 1.64 kg/m$^3\times$ m/s for maximum acoustic impedance attribute (red areas in Figure 5.8a). This arbitrary value will be used as a discriminator for locating carbonate buildups.

This concludes with the generation of the volume of broad-bandwidth acoustic impedance data from the band-limited seismic data and well log data. In the next section an estimation of porosities will be computed from the broad-bandwidth volume of acoustic impedance data.

5.1.3 Estimation of porosities

In order to estimate porosities from the broadband acoustic impedance volume a relationship between them should be established. Figure 5.9a shows a crossplot of the acoustic impedance log and neutron log for all wells in the study area as well as for the entire reservoir. The color scale corresponds to gamma-ray log. It can be observed that there are points off the general trend that also show high values of gamma-ray.

The well data was restricted to the productive zone. Figure 5.9b shows the data for the productive zone only. It can be seen that the data off the general trend were removed as well as those points showing high values of gamma-ray. Few points of high gamma-ray values can still be observed in the productive zone due to fact that carbonate buildups of Permian Basin pose some interbeded shales. With aid of the gamma-ray it can be determined that impermeable lithologies (high gamma-ray) have low acoustic impedance (8e6 kg/m$^3\times$ m/s $\sim$ 1.4e7 kg/m$^3\times$ m/s) and high porosity values (10% $\sim$ 30%), whereas permeable lithologies (low gamma-ray) have high acoustic impedance (1.4 kg/m$^3\times$ m/s $\sim$ 2.0 kg/m$^3\times$ m/s) and lower porosity values (0% $\sim$ 10%). The fact that impermeable formations show higher porosity than permeable ones, is probably attributed to the neutron log sensing bonded water present on it. The tool reads the hydrogen content and consequently, this content is proportional to porosity (Schlumberger, 1989). In general, porosity neutron logs generate some negative porosity values as seen in Figure 5.9, these porosities can be correlated to low porosity rocks with anidrite cements (Jensen personal communica-

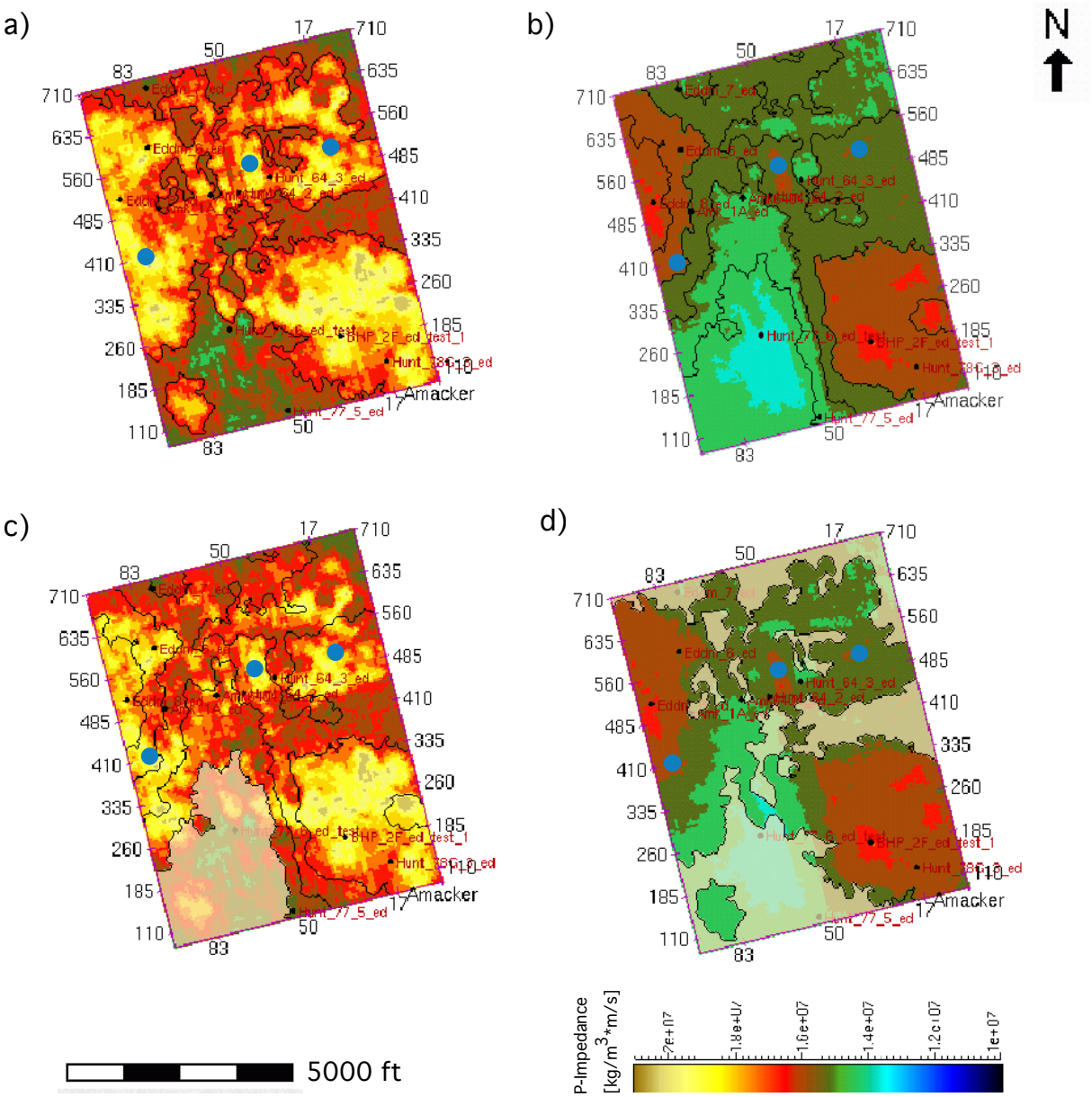

Fig. 5.8. Broadband acoustic impedance attributes across the productive zone. (a) maximum acoustic impedance attribute, (b) average (rms) acoustic impedance attribute. (c) low values of rms acoustic impedance (shaded areas) on top of maximum attribute, (d) low values of maximum acoustic impedance (shaded areas) on top of the rms attribute.

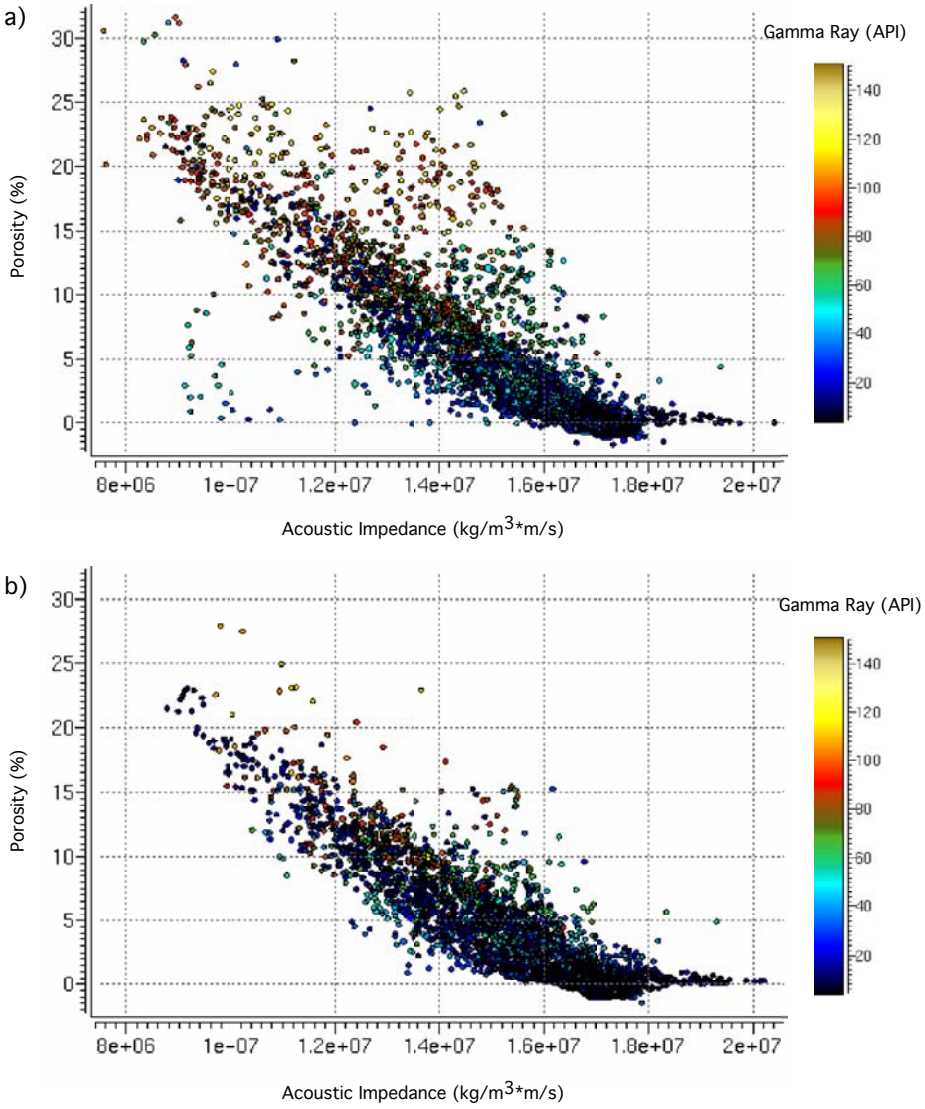

Fig. 5.9. Crossplot of the acoustic impedance log and neutron log for all wells in the study area for the (a) entire reservoir and (b) for productive zone only (Amacker formation).

tion). These results can be correlated with lithologies and formations present in the study zone. Impermeable lithologies (high gamma-ray) correspond to Tippet Shale and Wolfcampian-Leonardian shales located at the top and bottom of the reservoir zone respectively, whereas the permeable lithologies (low gamma-ray) correspond to the productive zone.

It is widely accepted that carbonate rocks tend to have complicated pore system. Different pore types have different compressibilities that strongly affect the seismic velocities. Not only the pore type and shape can change the velocity but also the mineral content (Wang, 1997). Thus, the large scatter of data observed in Figure 5.9b is probably due to the combination of different pore types. At equal porosities, velocities can vary up to 30%. This variation is caused by the ability of rocks to form cements and particular fabrics that enhances elastic properties (Anselmetti and Eberli, 1997).

Once the well data was analyzed for the depth of interest, a mathematical relation between the acoustic impedance log and neutron porosity log was determined. This relation was reached by crossplotting the acoustic impedance log and neutron porosity log for all wells independently in the study area and for the productive zone only. Well Amk_1A was not included in the study since porosity log was not available. These relations were achieved by computing a polynomial regression of second degree for each well in order to determine which well generates the best regression and trend. Figure 5.10a shows the regressions obtained for each well in the study area. It can be observed that wells Eddm_7, BHP_2F, Amk_6404 and Hunt_77_5 do not follow similar trends as all other wells in the study area. Even though wells Hunt_77_5 and Amk_6404 showed high correlation during the regression (more than 0.90), they were not considered during the first analysis. On the other hand, wells BHP_2F and Eddm_7 reached lower correlation values (less than 0.90). The first analysis was concentrated in estimating a regression for the six wells with similar trends and high correlation values (more than 0.90)(Figure 5.10b). Only these six wells were isolated and once more a regression was computed. This result is shown as a black curve in Figure 5.10c. The second analysis also shown in Figure 5.10c (blue curve) presents the regression computed for all wells including those with different trends and low correlation values. An additional analysis, not presented here, demonstrated the error between these two regressions to be less than 10%. Thus, a similar porosity volumes can be expected using these two regressions.

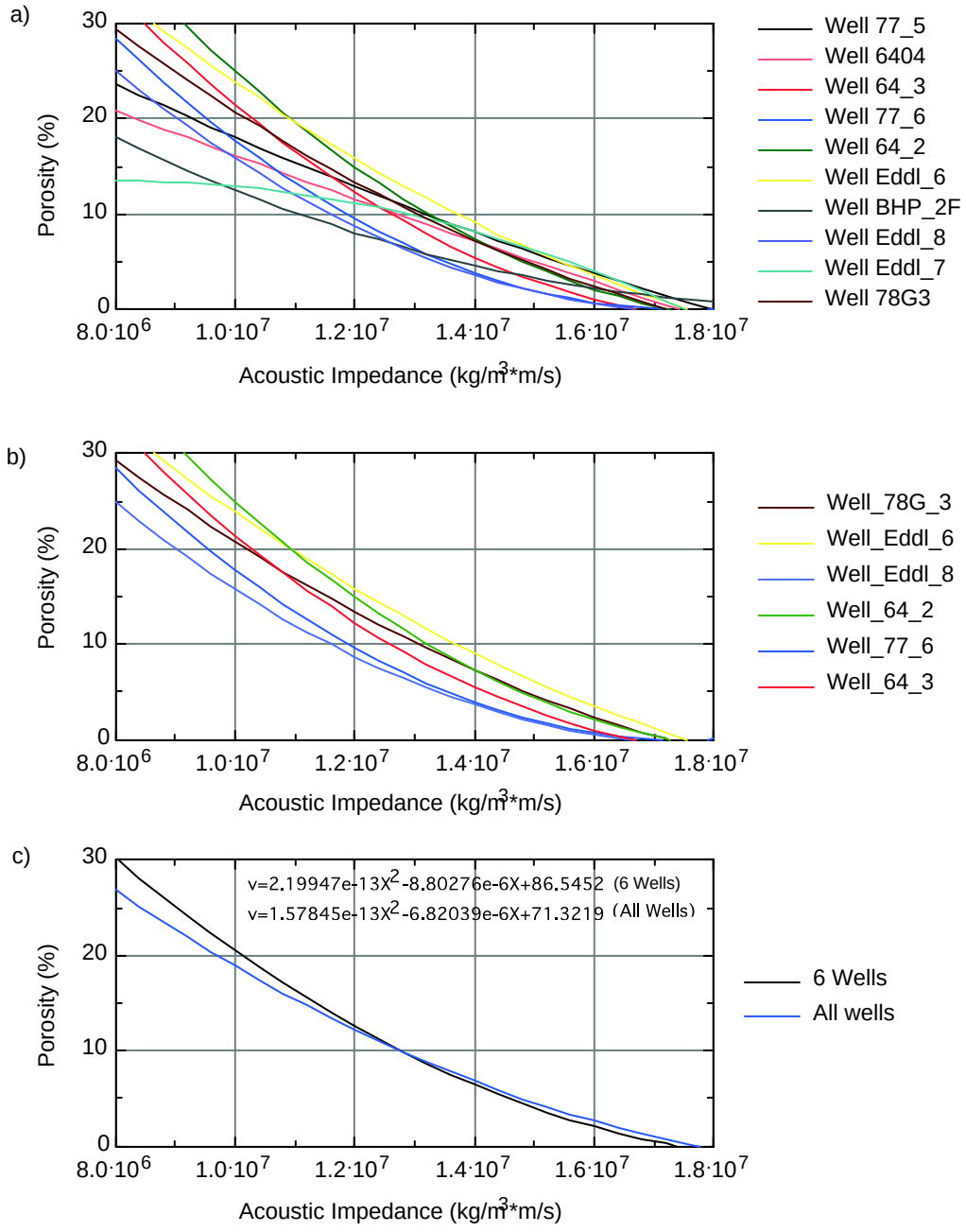

Fig. 5.10. Regression computed from acoustic impedance log and neutron porosity log. (a) for all wells, (b) for six wells. (c) average regression for all and six wells. Notice that both regressions are similar and will generate similar porosity volumes.

The data used to compute the regressions for all wells and the six isolated wells are shown in Figure 5.11a and 5.11b respectively. The regressions previously estimated will be used to extrapolate and compute a volume of porosities from the inverted broadband acoustic impedance volume. Essentially, the equation obtained from the regression is applied to each sample in each trace to compute the extrapolated value of porosity from the given acoustic impedance value. In order to quantify the porosity of the carbonate buildups, average (rms) maps for the productive zone were generated, as well as the difference between these two porosity maps (Figure 5.12). It is clear from the Figure 5.12a and 5.12b that the regression computed from all wells enhances porosity values, whereas the regression computed from six wells tends to generate lower porosities. This result could be predicted by studying Figure 5.10c where both regressions cross each other at 1.35e7 kg/m$^3\times$ m/s, and they separate toward higher values of acoustic impedance. Additionally, from the two porosity maps it can be observed that the lowest difference occurs on areas of low acoustic impedance (1.35e77 kg/m$^3\times$ m/s $\sim$ 1.50e7 kg/m$^3\times$ m/s) or high porosities (6% $\sim$ 10%), whereas, highest difference is correlated to areas of higher acoustic impedance (1.50e77 kg/m$^3\times$ m/s $\sim$ 1.60e7 kg/m$^3\times$ m/s) or lower porosities (1% $\sim$ 5%) (Figure 5.8 and Figure 5.12). The fact that the error or difference between them is negligible when compared to the range of theoretical values of porosities for carbonates (Anselmetti and Eberli, 1997) and (Mavko et al., 1998) led us to chose the model generated using all wells as the final porosity model.

5.2 Discussion of results

Generally, carbonates appear as mounded and drapped reflections in seismic sections. These patterns are difficult to recognize, making cumbersome its interpretation. Inversion of acoustic impedance helps to improve the imaging of these complex and discontinuous patterns. As previously shown, best results of inversion of acoustic impedance from input seismic data are achieved when an average wavelet from all individual wavelets generated during the tie process is used. The inversion is greatly improved when low frequency content of acoustic impedance from well data was added. This generated a more continuous and clearer image of the distribution of acoustic impedance and thus the geologic structure. The broadband acoustic impedance volume also enhances changes in physical properties, and therefore litho-

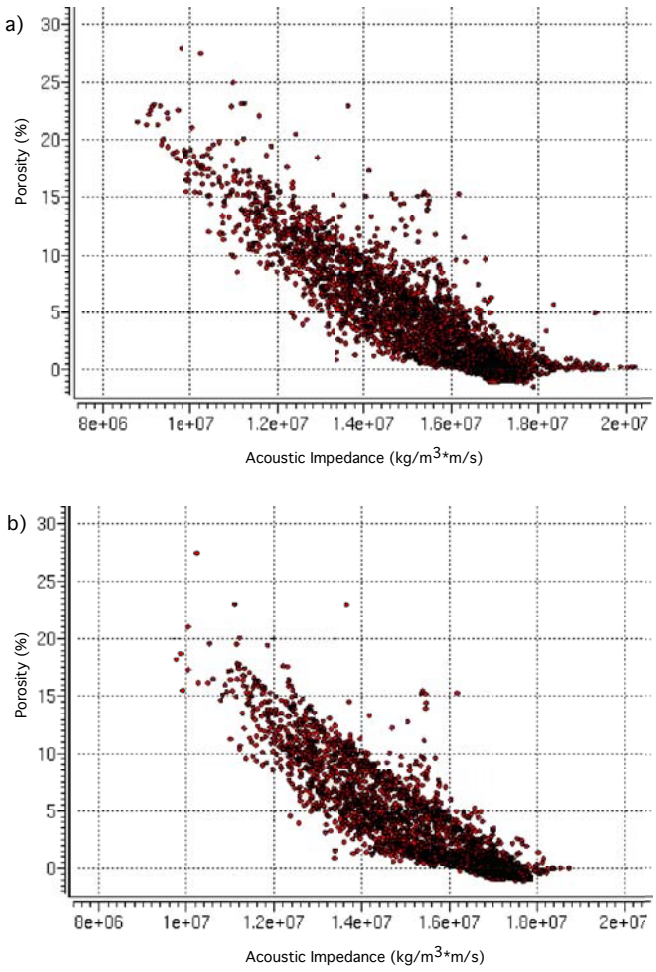

Fig. 5.11. Crossplots of the acoustic impedance log and neutron porosity logs for (a) all wells in the study area and (b) six wells. Both crossplots correspond to the productive zone.

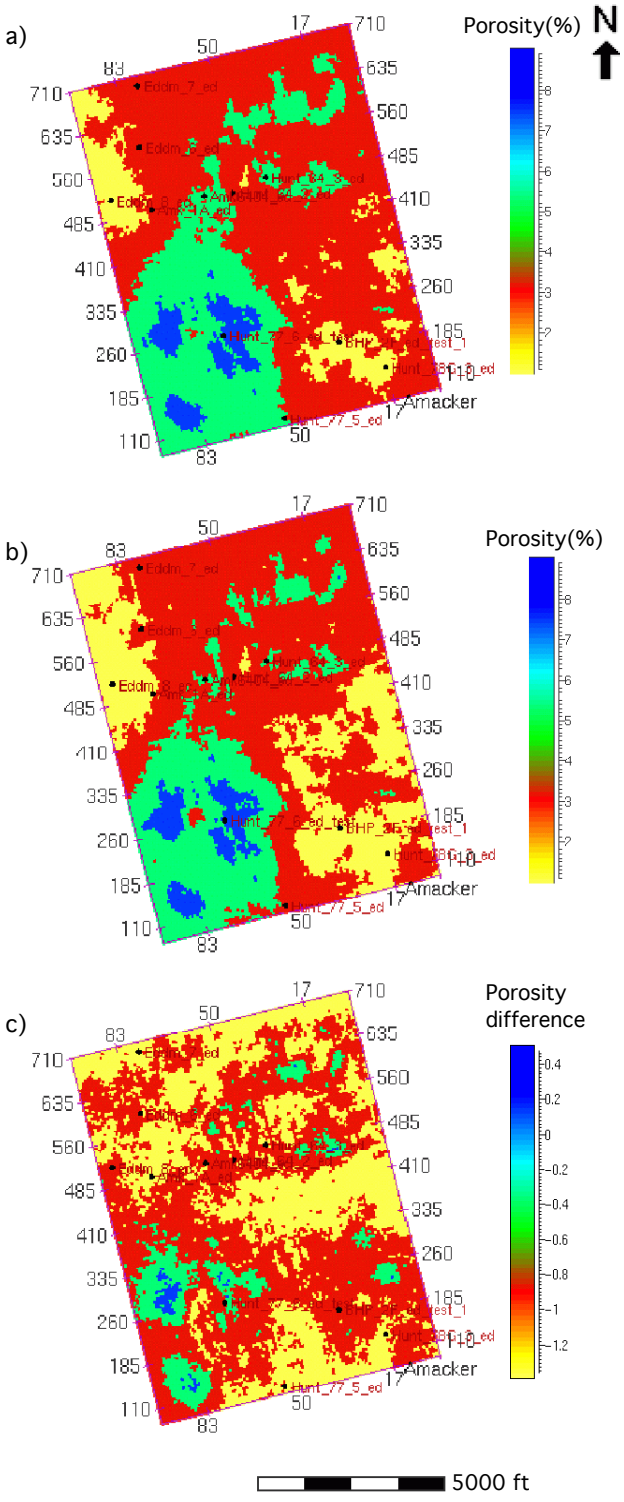

Fig. 5.12. Average (rms) maps of porosity generated using regressions for (a) all wells and (b) six wells. (c) Difference between average maps.

logic changes. Thus, improving the identification of carbonate buildups. With the aid of well data, the lithologic correlation from acoustic impedance is easy to establish and rock types can be inferred as well.

Figure 5.8c shows low values of average (rms) acoustic impedance (shaded area) on top of the maximum attribute map. Contrarily, Figure 5.8d shows low values of maximum acoustic impedance attribute (shaded areas) on top of the average (rms) attribute map. Those areas that share high acoustic impedance values (higher than 1.64 kg/m$^3\times$ m/s and 1.45 kg/m$^3\times$ m/s for maximum and rms acoustic impedance respectively) extracted from the depth of interest correspond to the location of the carbonate buildups. In fact, these results are confirmed with both the location of the current productive wells and results reported by Merriam (1999). Even though wells Eddm_7 and Hunt_77_5 are currently producing oil, they do not share both attributes. This is probably due to the fact that they are located close to the survey boundaries where seismic data have lower signal to noise ratio, and therefore the inversion of acoustic impedance is of lower quality. Well Amk_1A falls in a zone of low maximum acoustic impedance and high average (rms). Similarly, well Hunt_77_6 lies in an area of low acoustic impedance (rms and maximum). The fact that these locations do not share both acoustic impedance attributes probably explains why those wells are currently not producing.

Consequently, three new areas shown in Figure 5.8c and 5.8d can be suggested as possible productive carbonate buildups (blue dots). The first one is located in the northeastern part of the survey between crossline 485 and 560. The second zone is located on the western part of the survey on crosslines 410, and the third prospective zone is located in the center of the survey where crossline 500 intercepts inline 50. It is clear that these zones again share high values of acoustic impedance (maximum and rms). It is also important to mention that not only these three new suggested areas, but also current productive zones (well locations), are located on thicker zones as shown in the isopach map (Figure 5.13).

Decalf (2001) computed seismic attributes to determine the location of carbonate buildups. The variance attribute is reported to be the most effective one. The disadvantage of this technique is that it lacks of robustness and some specific parameters should be carefully tested and set to identify carbonate buildups. Inversion of acoustic impedance has proven to be more robust and reliable technique for identifying carbonate buildups. Even though buildups are not shown as particular or isolated

anomalies as reported by Decalf (2001), more continuous and detailed distribution of carbonate buildups is reported. Moreover, thickness of carbonate buildups are easier and more accurate to determine.

As previously explained, porosity in carbonate rocks has many origins, and they can comprise many type of pores. As shown in Figures 5.8 and 5.12 low values of acoustic impedance can be correlated to carbonates with high porosity, whereas high values of acoustic impedance are associated with carbonates containing low porosity. Figures 5.8 and 5.12 show that the wells Eddm_77_6 and Amk_1A (non-productive well) are located in a zone of low acoustic impedance and high porosity. In contrast, the rest of the wells share zones of high acoustic impedance and low porosity. An analysis performed by Anselmetti and Eberli (1997) of 295 carbonate cores shows that interparticle/intercrystalline, microporosity, moldic and intraframe porosity comprises a wide range of values. On the other hand, densely cemented carbonates tend to have lower porosities (Figure 3.3). The results reported in this study suggest that areas of high acoustic impedance are densely cemented with low porosity values ($0\% \sim 5\%$). Contrarily, areas with low acoustic impedance can be correlated to carbonates with interparticle/intercrystalline porosity, microporosity, moldic and intraframe porosity, and consequently higher porosities. Merriam (1999) also reported similar values of porosities for carbonate buildups in this area and pointed out that well Amk_1A has penetrated a carbonate debris buildup. It can be observed from Figure 2.3 that carbonate debris buildups tend to produce less than skeletal sand buildups. A detailed analysis of well log data for wells Eddm_77_6 and Amk_1A (mainly in gamma-ray logs) shows that in the zone of interest the log response is less regular than for productive wells. This suggests that probably interbeded shales are found along the zone of interest interrupting the connectivity of the pores and therefore generating low values of permeability. This is consistent with production tests done on these wells, where low rates of production of brine and hydrocarbons were obtained.

Along with the fact that well Hunt_77_6 is located in a zone of low acoustic impedance, there are also other factors that need to be considered to explain the reason why this well it is not producing (dry). Merriam (1999) mention that Tippet Shale is the source rock and seal for petroleum of carbonate buildups in Amacker area. At well Hunt_77_6, Tippet Shale is only 50 ft thick, whereas its thickness increases at the rest of the wells ($100 \sim 160$ ft). This fact suggests that either the thickness was not enough to produce oil or it is not an effective seal in this area. Figure 5.13 also

shows that the thickness of the Amacker formation at this location is considerably less than that at the rest of the wells. It is well known that carbonate buildups in the Permian Basin are characterized by a wide network of fractures. In addition to the fractures, porosity is created by diagenesis, and permeability is also enhanced by extensive fractures. This helps to connect separated buildups (Merriam, 1999). An analysis on seismic sections not shown here demonstrated that an extensive system of fractures are present in well Hunt_77_6, whereas minor faults are seen in wells Hunt_78G_3, BHP_2F and Hunt_77_5. This suggests that high porosity, along with extensive fractures, can act as migration channels.

Merriam (1999) reported two types of carbonate buildups based on analysis of cores, logs and seismic data. The distribution of carbonate buildups was determined by the paleotopography of the Strawn formation (Merriam, 1999). Specifically, Merriam (1999) mentions that skeletal sand carbonate buildups were grown in paleolows of Strawn formation and comprise thicker areas of the Amacker formation. In contrast, carbonate debris buildups were originated in paleohighs of the Strawn formation and correlate to thinner areas of the Amacker formation. The inversion of acoustic impedance was not able neither to distinguish between these two types of carbonate buildups, nor to stablish the origin of them. However, an isopach map of the Amacker formation generated with the aid of inverted acoustic impedance, input seismic data and well logs, has shown that all carbonate buildups are located on thick zones (Figure 5.13). In fact, thick areas of the Amacker formation correlate to areas of high acoustic impedance and low porosities. The inversion has also shown to be robust for estimating a distribution of porosities in the area.

5.3 Theoretical analysis

In order to confirm results presented here, theoretical values of density and acoustic impedance were computed for Time-Average and Gassmann's equations applying the Monte Carlo optimization algorithm. These parameters were computed as a function of porosity to correlate them with results presented in this study. Physical properties of fluids, minerals (dolomite) and rock matrix (limestone) were taken from literature (Mavko et al., 1998; Schön, 1996; Carmichael, 1982).

The inverted values of acoustic impedance were obtained using the Time-Average equation (3.33) and bulk density (3.36). The equation was written in terms of porosity,

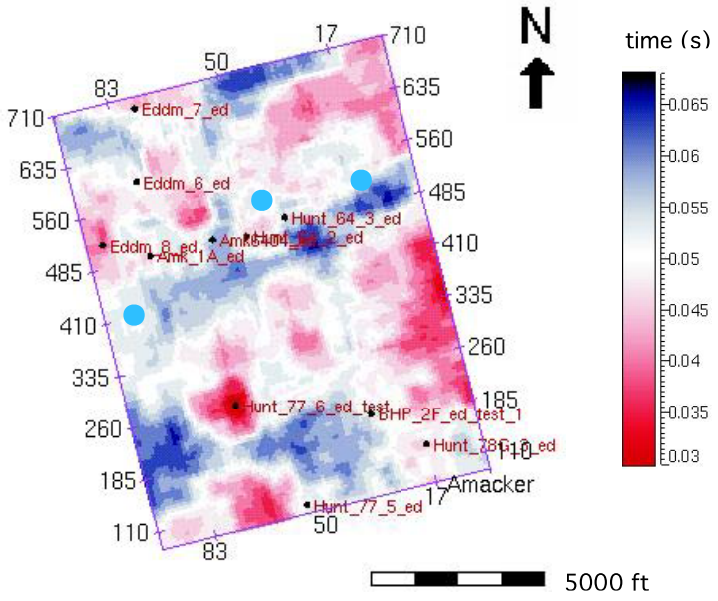

Fig. 5.13. Isopach map of the Amacker formation.

matrix and fluid velocity. Parameters inverted for this equation are shown in table 5.1.

Table 5.1. Parameters inverted in Time-average equation.

Wells	Matrix velocity (km/s)	Fluid velocity (km/s)	Matrix density (gg/cc)	Fluid density (gg/cc)
Productive	6.00 ± 0.06	1.96 ± 0.07	2.866	1.073
Non-productive	5.51 ± 0.04	1.68 ± 0.12	2.866	0.85

Figure 5.14 shows theoretical values of density (equation 3.36) and acoustic impedance as a function of porosity for different fluids (brine and oil). It can be observed that density (Figure 5.14a) is nearly constant for our range of porosity. On the other hand, acoustic impedance (Figure 5.14b) decrease linearly as porosity increases.

In general, V_p and V_s decrease with increasing porosity. This is due to a decrease in bulk and shear moduli with increasing porosity. These results are expected, since velocities are proportional to these moduli and they vary faster than the density. Consequently, this produces the decrease in velocity and therefore acoustic impedance

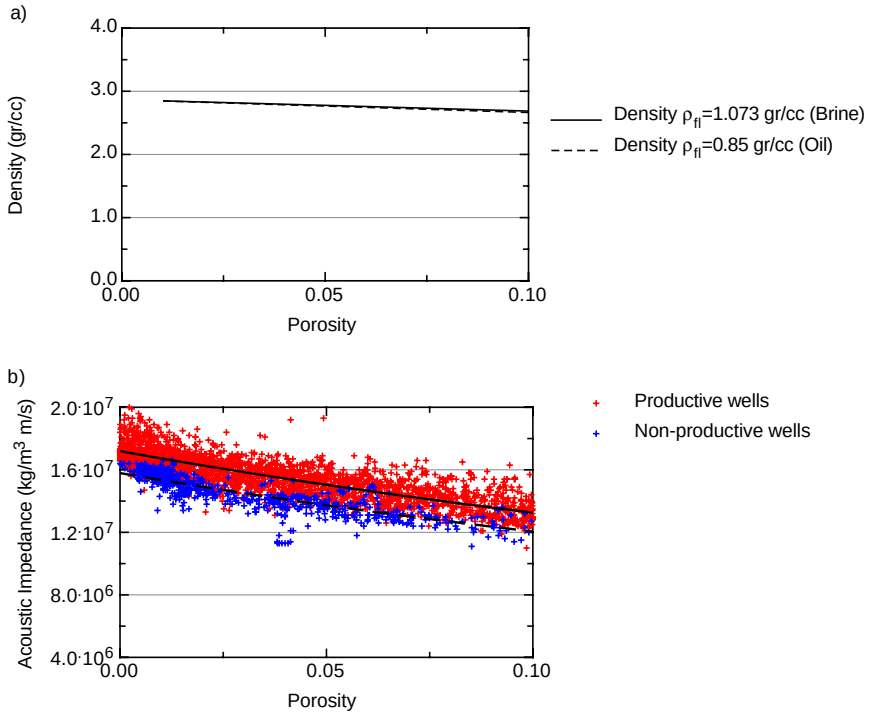

Fig. 5.14. (a) Density and (b) inverted acoustic impedance as a function of porosity using the time average equation for different fluids: brine and oil. Inverted parameters are shown in Table 5.1

observed in Figure 5.14b.

The solid curve represents the inverted equation for the productive wells, whereas the dashed line corresponds for non-productive wells. The inverted velocity values (Table 5.1) show that the velocity of the matrix and fluid are slightly higher for productive wells than for non-productive wells.

Carbonate rocks with intercrystalline or interparticle porosity are better described by the Time-Average equation (Saleh and Castagna, 2004). These rocks usually have porosity values of 0.3 ± 0.2. On the other hand, densely cemented rocks have lower porosity values 0.05 ± 0.05 (Anselmetti and Eberli, 1997). Inversion results from seismic data show that average porosity values in the study area are $0\% \sim 10\%$, typical for densely cemented rocks. This suggests that Time-Average equation will overestimate porosity values. The assumptions regarding the rock properties applied in the derivation of the Gassmann equation are violated if rock framework comprises multiple minerals, or if there is any anisotropic mineral framework. Previous studies reported that carbonate buildups in the study area are composed of moderately

to well-sorted grains and porosity is mainly moldic and leached porosity (Merriam, 1999). Therefore the Gassmann approach will be suitable for predicting the observed data.

The Gassmann relationship was used again to compute theoretical values of saturated bulk modulus (equation 3.34) and acoustic impedance (equations 3.35 and 3.36) as a function of porosity. Parameters inverted for this equation are shown in table 5.2. Figure 5.15 shows the sensitivity of the Gassmann equation (K_{sat}) for the mineral bulk modulus (K_o), fluid bulk modulus (K_{fl}) and the frame bulk modulus (K^*). It can be observed that the equation is highly sensitive to the frame bulk modulus, whereas for fluid and mineral bulk modulus is nearly constant. This can be clearly seen on the adding term corresponding to K^* in equation 3.34. Therefore we expect that acoustic impedance is also sensitive to the rigidity modulus as shown in equation 3.35.

Table 5.2. Parameters inverted in Gassmann equation.

Wells	K^* (GPA)	K_{fl} (GPA)	K_o (GPA)	G (GPA)
Productive	43.43 ± 6.04	1.84 ± 0.12	93.84 ± 7.14	17.46 ± 2.35
Non-productive	30.25 ± 2.77	2.83 ± 0.29	84.15 ± 5.38	12.69 ± 2.98

Previous results show that the inverted acoustic impedance using the Gassmann equation is sensitive to frame bulk modulus and therefore the rigidity modulus. Figure 5.16 shows the effect of these two parameters in the estimation of the acoustic impedance. It can be observed that as the frame bulk modulus increases the V_p/V_s ratio also increases. However, as the rigidity modulus increases the V_p/V_s ratio decreases. Since the lithology of the carbonate buildups is known (limestones), we assume that the $V_p/V_s = 1.9$. This parameter was used as a constraint during the inversion process. Figure 5.16a shows results when the value of rigidity G is fixed at 20 GPa, while Figure 5.16b is for inversion results when $G = 40$ GPa. The best inversion result for $G = 20$ is for $V_p/V_s = 1.957$, while for $G = 40$ it is $V_p/V_s = 1.443$. Though the fit is equally good, the latter produces an unrealistic V_p/V_s ratio. Inverted results (Figure 5.16c) (Table 5.2) shows that productive reservoir rocks have higher frame and rigidity moduli than non-productive rocks. It also shows that fluid bulk

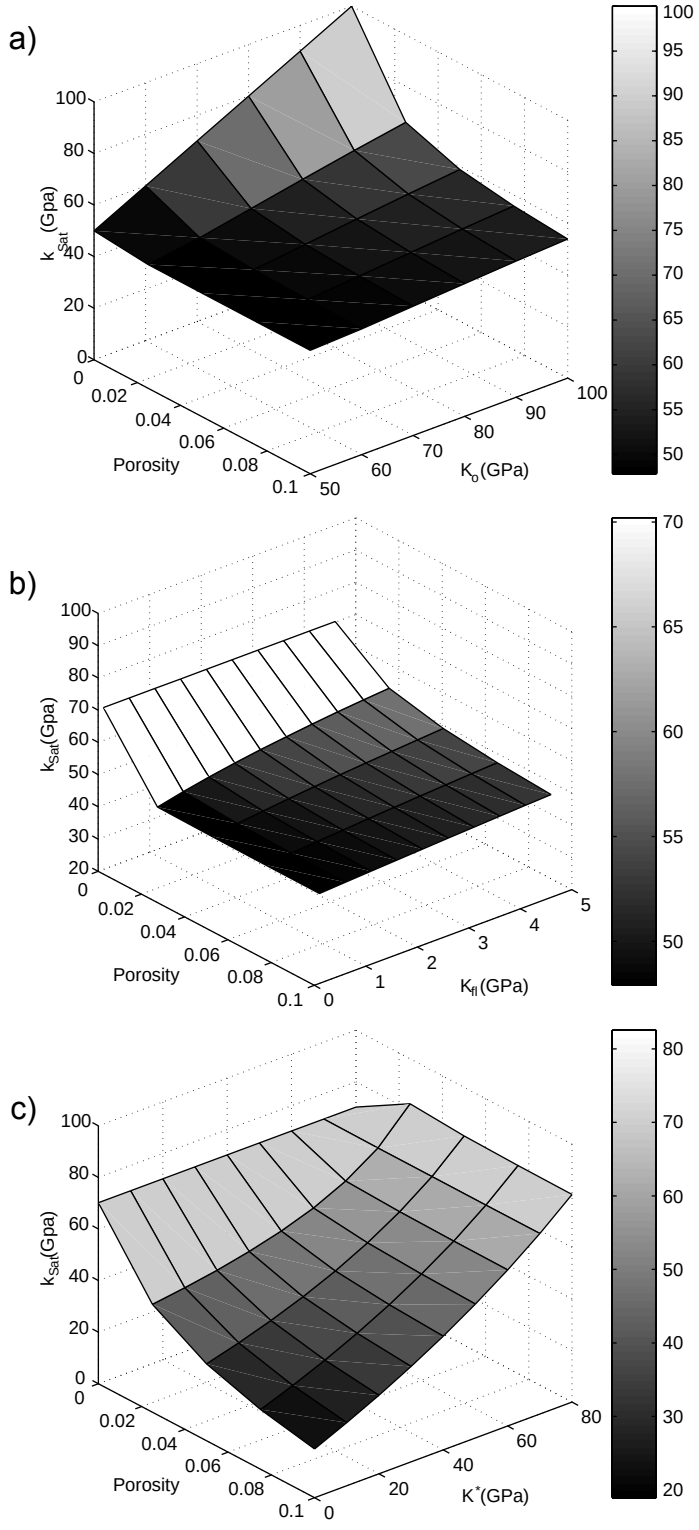

Fig. 5.15. Sensitivity of the Gassmann equation (K_{sat}) as a function of porosity (a) mineral bulk modulus (K_o), (b) fluid bulk modulus (K_{fl}) and (c) frame bulk modulus (K^*)

.

modulus for the productive wells is slightly higher than for non-reservoir rocks which can be correlated with oil and brine, respectively. This is consistent with current production data.

In general both approaches validated results previously reported. This is, a decrease in compressional velocity and acoustic impedance as porosity increases. Usually when rocks are filled with a less compressible fluid, the compressibility of the rock decreases and thus, the velocity increases. In addition, the mineral content can also affect the compressional velocity. For instance, dolomites and anhydrite in limestone increase V_p while sand decreases it. However, the pore geometry is the principal factor that controls the increase in V_p. For high aspect pore ratio the compressibility is low and the pore compressibility does not depend on pore fluid. On the contrary, for low aspect pore ratio (cracks or microcracks), the pores are very compressible resulting in a dramatic increase of V_p (Wang et al., 1991).

As observed, the acoustic impedance inversion is a robust method for determining a detailed distribution of changes in acoustic impedance. In fact, it can be used on thin layers where the conventional seismic data lack of enough resolution to resolve changes of physical properties. The study presented here shows that inversion of acoustic impedance was able to resolve the location of carbonate buildups and provided reliable estimation of porosities. In addition, with the aid of theoretical models, distribution of porosities were confirmed and fluid filling were inferred as well. It is mandatory for the inversion to have at least one well with acoustic impedance log to extract the low frequency component. It is then clear, that this inversion highly depends on the numbers of available wells and the quality of the data. Similarly, the inversion of acoustic impedance greatly depends on both the quality of the input seismic data and the selected wavelet.

As reported, those areas with high acoustic impedance (maximum and average) and low porosities (less than 5%) are suggested as prospective drilling targets. A relation of acoustic impedance and porosity helps to understand the distribution of porosities in carbonates buildups. It is clear from previous results that there is a strong correlation between the inverted acoustic impedance and the porosity model since the same data (acoustic impedance logs) are used for both results. In order to overcome this issue and validate the inversion even more, it would be necessary to extract the low frequency component from the velocity model obtained during processing of seismic data. In order to confirm results presented here it would be

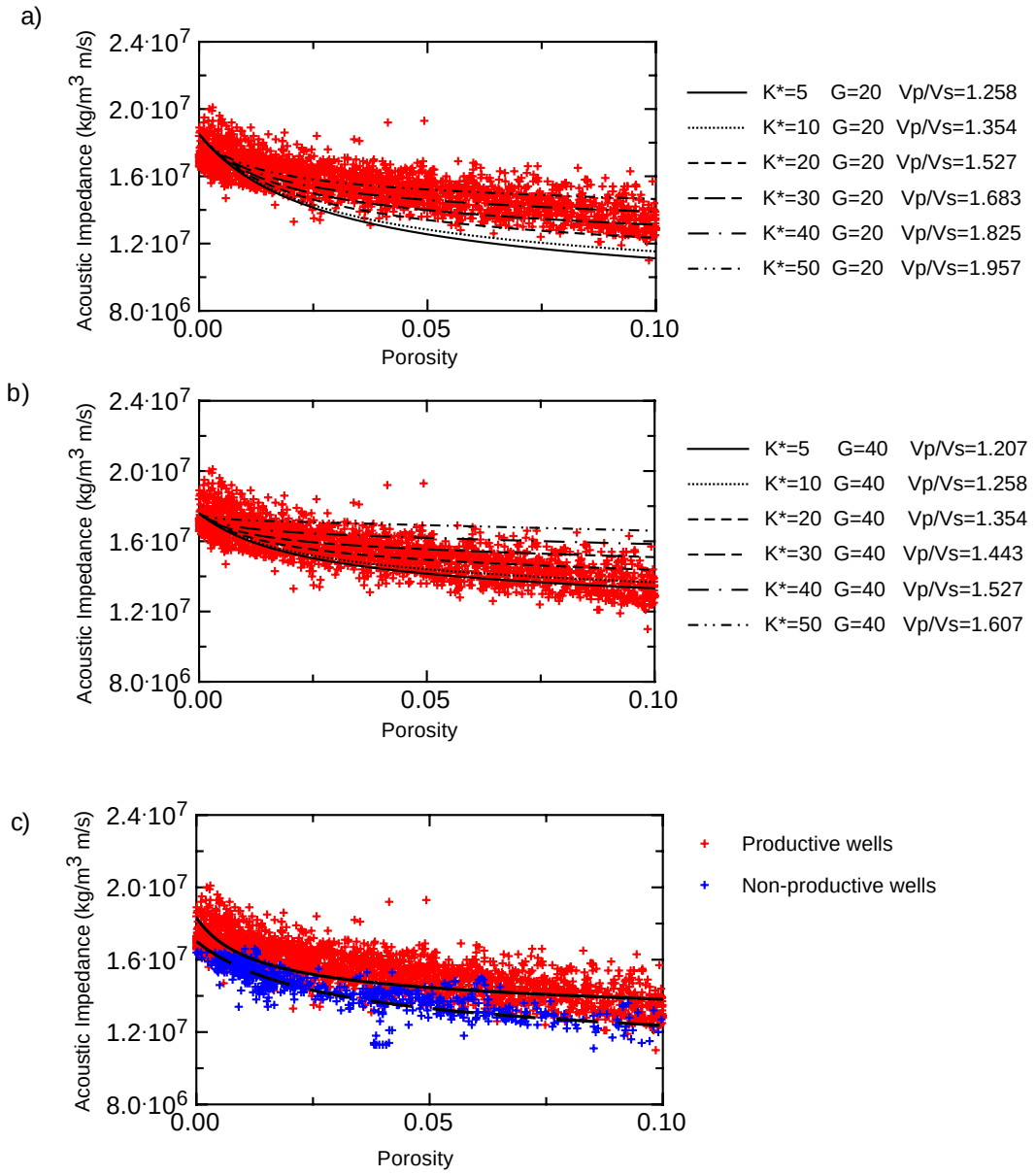

Fig. 5.16. Results of the inversion of impedance as a function of porosity for productive wells. The red and blue points are data for productive and non-productive wells respectively, and the black curves are several inversion results. (a) G fixed at 20 GPa, (b) G fixed at 40 GPa and (c) inverted results for productive and non productive wells. Inverted parameters are shown in Table 5.2.

important to apply the inversion in the King Mountain seismic survey (North of Amacker survey) which includes the well well Eddm_7 which is located in the border of Amacker survey.

CHAPTER VI

CONCLUSIONS

The inversion of acoustic impedance showed to be and efficient, fast and robust method to image and determine the location of carbonate buildups in the Permian Basin. This method is efficiently applicable in complex areas, as well as in thin layers, where conventional seismic data are not able to resolve them.

The inversion of acoustic impedance, and therefore the proper interpretation of it, depends in great extent to the selection of the wavelet used during the inversion process and the quality of the input seismic data. Results showed that the inversion is sensitive to these parameters. Using an incorrect wavelet, wrong values of acoustic impedance will be obtained. Thus, a wavelet properly extracted from the tie process that best characterizes the seismic data should be used.

The inversion of band-limited seismic data also generated a band-limited acoustic impedance volume. This band-limited model does not contain low frequency content which improves the temporal resolution. Results showed that this band-limited model does not resolve properly the distribution of acoustic impedance. Only the maximum acoustic impedance attribute showed a poor detailed distribution of them. Similarly, average (rms) acoustic impedance showed no consistent results. Adding low frequency content from the geological model a broadband acoustic impedance volume is generated that greatly improved these results. Thus, maps of maximum and average (rms) attributes, showed a clear and more detailed distribution of acoustic impedance in the study area.

Areas with high acoustic impedance (maximum and average) suggest the presence of carbonate buildups. These locations correlate with both current producing wells and results presented by Merriam (1999). Areas of low acoustic impedance do not correlate with productive wells.

A second degree polynomio was obtained as the best relationship between both the acoustic impedance log and the neutron porosity log. With this relationship, areas of low porosities were correlated with high acoustic impedance values and areas of high porosities were associated with low acoustic impedance.

Additionally, results of the isopach map of the productive formation showed that

current productive carbonate buildups are located in thick areas of high acoustic impedance and low porosity. Contrarily, thinner zones of the productive formation correlate to non-productive carbonate buildups, with low acoustic impedance and high porosity values. Those carbonates, are subjected to extensive fractures and high permeabilities, generating migration channels, and consequently, resulting in non-economical reservoirs. An extension of these results allowed us to propose three new locations for prospective carbonate buildups.

Theoretical models helped to validate and predict results obtained during the acoustic impedance inversion. Gassmann approach describes better the measured data. This model confirmed previous inverted results obtained from seismic data and helped to estimate rock property values that are consistent with current data. Both the inverted seismic and well data failed to determine the origin and type of carbonate buildups.

The method presented here depends extensively on the quality of the seismic data and the well log data as well. At least one well with an acoustic impedance log is required to generate the broadband acoustic impedance model. This clearly shows the existing compromise between the quality of the inverted acoustic impedance data and the available well log data. Additionally, a strong correlation between the acoustic impedance and porosity is expected, since acoustic impedance logs were used for generating both the low frequency acoustic impedance model and the porosity volume. A volume of velocities generated during seismic processing would break the existing correlation, improving the generation of broadband acoustic impedance volume and estimation of porosities.

REFERENCES

Anselmetti, F. S., and Eberli, G. P., 1997, Sonic velocities in carbonate sediments and rocks, *in* Palaz, I., and Marfurt, K. J., Eds., Carbonate seismology: Society of Exploration Geophysicists, Geophysical Developments, 53–74.

Badley, M. E., 1985, Practical seismic interpretation: International Human Resources Development Corporation.

Becquey, M., Lavergne, M., and Willm, C., 1979, Acoustic impedance logs computed from seismic traces: Geophysics, **44**, 1485–1501.

Berteussen, K. A., and Ursin, B., 1983, Approximate computation of the acoustic impedance from seismic data: Geophysics, **48**, 1351–1358.

Biot, M., 1956, Theory of propagation of elastic waves in fluid saturated porous solid,I. low frequency range: J. Acoust. Soc. Am., **28**, 168–191.

Carmichael, R. S., 1982, Handbook of physical properties of rocks: CRC Press.

Cornish, B. E., and King, G. A., 1988, Combined interactive analysis and stochastic inversion for high-resolution reservoir modeling: Presented at the 50th Mtg., European Assn. Expl. Geophys.

Debeye, H. W., and van Riel, P., 1990, l_p *norm* deconvolution: Geophys. Prosp., **38**, 381–403.

Decalf, C., 2001, Seismic attribute analysis of lower Permian Wolcampian - Leonardian carbonate buildups, S.W.Midland, Texas: M.S. thesis, Texas A&M University.

Fullagar, P. K., 1985, Spike recovery deconvolution, *in* Fitch, A. A., Ed., Developments in geophysical exploration methods: Elsevier Applied Science, 6, 1–25.

Graebner, R., and Wason, H. M., 1981, Three dimensional methods in seismic exploration: Science, **211**, 535–540.

Hardage, B. A., 1987, Seismic stratigraphy: Geophysical Press.

Jason Geoscience Workbench, 2002, Unpublished training manual: Trace based inversion and modeling: Fugro - Jason. Houston, Texas.

Levy, S., and Fullagar, P. K., 1981, Reconstruction of a sparse spike train from a portion of its spectrum and application to high resolution deconvolution: Geophysics, **46**, 1235–1243.

Li, Y., and Downton, J., 2000, The application of amplitude versus offset in carbonate reservoirs: Re-examing the potential: 70th Ann. Internat. Mtg., Soc. Expl. Geophys. Expanded Abstracts, 166–169.

Ma, X. Q., 2001, A constrained global inversion method using an overparameterized scheme: Application to poststack seismic data: Geophysics, **66**, 613–626.

Madiba, G. B., and McMechan, G. A., 2003, Seismic impedance inversion and interpretation of gas carbonate reservoir in the Alberta Foothills, western Canada: Geophysics, **68**, 1460–1469.

Mavko, G., Mukerji, T., and Dvorkin, J., 1998, The rock physics handbook: Cambridge University Press.

McCunn, H. J., and Walker, R. D., 1962, General geologic relationship between outcrops of the Diablo Plateau region and the subsurface of the Permian Basin of West Texas, *in* Leonardian facies of the Sierra Diablo region, West Texas: Field trip guidebook: SEPM Special Publication 62.

Merriam, C. O., 1999, Depositional history of lower Permian (Wolfcampian - Leonardian) carbonate buildups, Midland Basin,Upton County, Texas: M.S. thesis, Texas A&M University.

Oldenburg, D. W., Scheuer, T., and Levy, S., 1983, Recovery of the acoustic impedance from reflection seismograms: Geophysics, **48**, 1318–1337.

Palaz, I., and Marfurt, K. J., 1997, Carbonate seismology: An overview, *in* Palaz, I., and Marfurt, K. J., Eds., Carbonate seismology: Society of Exploration Geophysicists, Geophysical Developments, 1–7.

Russell, B. H., 1988, Introduction to seismic inversion methods: Course Notes Series:, volume 2 Society of Exploration Geophysicists.

Saleh, A. A., and Castagna, J. P., 2004, Revisiting the Wyllie time average equation in the case of near-spherical pores: Geophysics, **69**, 45–55.

Schlumberger, 1989, Log interpretation. Principles and applications: Schlumberger Educational Services.

Schön, J. H., 1996, Physical properties of rocks: Geophysical Press.

Smith, T. M., Sondergeld, C. H., and Rai, C. S., 2003, Gassmann fluid substitutions: A tutorial: Geophysics, **68**, 430–440.

Tai, P. C., 2001, Late paleozoic foreland deformation in the Southwestern Midland Basin and adjacent areas: Implications for tectonic evolution of the Permian Basin, West Texas: Ph.D. dissertation, Texas A&M University.

Taylor, H. L., Banks, S. C., and McCoy, J. F., 1979, Deconvolution with the l_1 *norm*: Geophysics, **44**, 39–52.

Wang, Z., Hirsche, W. K., and Sedgwick, G., 1991, Seismic velocities in carbonate rocks: Journal of Canadian Petroleum Technology, **30**, 112–122.

Wang, Z., 1997, Seismic properties of carbonate rocks, *in* Palaz, I., and Marfurt, K. J., Eds., Carbonate seismology: Society of Exploration Geophysicists, Geophysical Developments, 29–52.

White, R. E., 1980, Partial coherence matching of synthetic seismograms with seismic traces: Geophys. Prosp., **28**, 333–358.

Wilson, J. L., 1975, Carbonate facies in geologic history: Springer-Verlag.

——— 1997, Carbonate depositional enviroments and diagenesis, *in* Palaz, I., and Marfurt, K. J., Eds., Carbonate seismology: Society of Exploration Geophysicists, Geophysical Developments, 9–28.

Yang, K. M., and Dorobek, S. L., 1995a, The Permian Basin of west Texas and New Mexico: Flexural modeling and evidence for lithospheric heterogeneity across the Marathon foreland, *in* Dorobek, S. L., and Ross, Eds., Stratigraphic evolution of foreland basins: Society for Sedimentary Geology, Special Publication 52.

——— 1995b, The Permian Basin of west Texas and New Mexico: Tectonic history of a 'composite' foreland basin and its effects on stratigraphic developments, *in* Dorobek, S. L., and Ross, Eds., Stratigraphic evolution of foreland basins: Society for Sedimentary Geology, Special Publication 52.

VITA

Pablo Buenafama Aleman

Permanent address

Department of Geology and Geophysics

Texas A&M University

College Station, Texas 77843

979-458-1169

Education

M.S., May 2004, Texas A&M University, Department of Geology and Geophysics.

B.S., January 1999, Simon Bolivar University, Department of Earth Sciences. Caracas, Venezuela. Thesis: Estimation of velocities and angles of incidence in anisotropic media using VSP multicomponent data. Major Geophysics.